The impact of baryons on massive galaxy clusters: halo structure and cluster mass estimates

Monique A. Henson,[1][*] David J. Barnes,[1] Scott T. Kay,[1] Ian G. McCarthy[2] and Joop Schaye[3]

[1]*Jodrell Bank Centre for Astrophysics, School of Physics and Astronomy, The University of Manchester, Manchester M13 9PL, UK*
[2]*Astrophysics Research Institute, Liverpool John Moores University, 146 Brownlow Hill, Liverpool L3 5RF, UK*
[3]*Leiden Observatory, Leiden University, PO Box 9513, NL-2300 RA Leiden, the Netherlands*

ABSTRACT

We use the BAHAMAS (BAryons and HAloes of MAssive Systems) and MACSIS (MAssive ClusterS and Intercluster Structures) hydrodynamic simulations to quantify the impact of baryons on the mass distribution and dynamics of massive galaxy clusters, as well as the bias in X-ray and weak lensing mass estimates. These simulations use the subgrid physics models calibrated in the BAHAMAS project, which include feedback from both supernovae and active galactic nuclei. They form a cluster population covering almost two orders of magnitude in mass, with more than 3500 clusters with masses greater than $10^{14}\,\mathrm{M_{\odot}}$ at $z = 0$. We start by characterizing the clusters in terms of their spin, shape and density profile, before considering the bias in both weak lensing and hydrostatic mass estimates. Whilst including baryonic effects leads to more spherical, centrally concentrated clusters, the median weak lensing mass bias is unaffected by the presence of baryons. In both the dark matter only and hydrodynamic simulations, the weak lensing measurements underestimate cluster masses by ≈ 10 per cent for clusters with $M_{200} \leq 10^{15}\,\mathrm{M_{\odot}}$ and this bias tends to zero at higher masses. We also consider the hydrostatic bias when using both the true density and temperature profiles, and those derived from X-ray spectroscopy. When using spectroscopic temperatures and densities, the hydrostatic bias decreases as a function of mass, leading to a bias of ≈ 40 per cent for clusters with $M_{500} \geq 10^{15}\,\mathrm{M_{\odot}}$. This is due to the presence of cooler gas in the cluster outskirts. Using mass weighted temperatures and the true density profile reduces this bias to 5–15 per cent.

Key words: gravitational lensing: weak – galaxies: clusters: general.

1 INTRODUCTION

Galaxy clusters are a sensitive probe of the late time evolution of the Universe, providing crucial insights into the nature of both dark matter and dark energy. Cluster-based cosmological tests require well-constrained masses for large samples of clusters. There is a long standing debate about the bias in X-ray cluster masses (see Mazzotta et al. 2004; Rasia et al. 2012; Applegate et al. 2014; Smith et al. 2016), which arises due to the assumption that clusters are in hydrostatic equilibrium. Since clusters are often unrelaxed systems, this is frequently not a valid assumption. Instead, many authors are moving towards using masses derived from weak lensing (WL) observations of clusters (Okabe et al. 2010; Mahdavi et al. 2013; Hoekstra et al. 2015; Kettula et al. 2015) or at the very least, calibrating X-ray masses using WL measurements (e.g. Lieu

et al. 2016). The power of cluster counting has been highlighted in Sunyaev–Zel'dovich surveys performed by the *Planck* satellite (Planck Collaboration XXIV 2016) and the South Pole Telescope (SPT; Bocquet et al. 2015), however more accurate cluster mass measurements are needed for cluster cosmology to be competitive with other techniques (Allen, Evrard & Mantz 2011; Planck Collaboration XXIV 2016). High-quality observational data are forthcoming with the ongoing and upcoming Dark Energy Survey (The Dark Energy Survey Collaboration 2005), SPT-3G (Benson et al. 2014), Large Synoptic Sky Survey (Ivezic et al. 2008) and ACTpol (Niemack et al. 2010), but we also need simulations to provide robust theoretical predictions for comparison, as well mock data for testing observational techniques.

Galaxy clusters have been extensively studied in dark matter only (DMO) simulations. It is well established in those simulations that cold dark matter (CDM) haloes are triaxial, prolate structures. The sphericity of dark matter haloes decreases with increasing mass, so that galaxy clusters typically have sphericities of

$(c/a) \simeq 0.4$–0.6 (Macciò, Dutton & van den Bosch 2008; Muñoz-Cuartas et al. 2011; Bryan et al. 2013). Since both concentration and spin have also been shown to decrease weakly with mass (Bett et al. 2007; Duffy et al. 2008; Klypin, Trujillo-Gomez & Primack 2011; Muñoz-Cuartas et al. 2011; Ludlow et al. 2012; Klypin et al. 2016), high-mass clusters typically have low concentrations and exhibit little rotational support.

DMO simulations have also been instrumental in testing observational methods for measuring cluster masses. Weak gravitational lensing provides a promising method for measuring the masses of galaxy clusters, since it does not require any assumptions about the dynamical state of the cluster. DMO simulations have shown that WL masses are typically biased low by ∼5 per cent, with this bias decreasing with increasing mass (Becker & Kravtsov 2011; Oguri & Hamana 2011; Bahé, McCarthy & King 2012). Understanding this bias is crucial for cluster cosmology, since it requires large samples of clusters with accurately determined masses.

Cosmological hydrodynamic simulations have shown that including baryons can have a significant effect upon the mass distribution of groups and low-mass clusters (e.g. Bryan et al. 2013; Cusworth et al. 2014; Velliscig et al. 2014; Schaller et al. 2015). The inclusion of baryonic effects in cosmological simulations leads to the depletion of high-mass clusters (Cusworth et al. 2014), and the clusters that do form are more spherical and have higher concentrations than their DMO counterparts (Duffy et al. 2010; Bryan et al. 2013). The baryon fraction and hence the total mass within clusters are sensitive to galaxy formation processes (Stanek, Rudd & Evrard 2009; McCarthy et al. 2011; Martizzi et al. 2012; Le Brun et al. 2014; Velliscig et al. 2014).

Thus, the impact of baryons on the shape and density profile of clusters depends on galaxy formation efficiency (Duffy et al. 2010; Bryan et al. 2013). The impact of baryons on the mass distribution of low-mass clusters is not just limited to the central regions of clusters; feedback from active galactic nuclei (AGNs) can alter low-mass cluster profiles out to R_{200} (Velliscig et al. 2014).[1] It is still unclear what effect baryons will have on high-mass clusters. If baryons have a significant impact on the mass distribution of massive galaxy clusters, this may have implications for mass estimation techniques such as cluster WL, which have been tested on DMO simulations (Becker & Kravtsov 2011; Oguri & Hamana 2011; Bahé et al. 2012).

The lack of hydrodynamic simulations of massive galaxy clusters is a natural consequence of the large computational cost of such simulations. Furthermore, accounting for baryonic effects is not a trivial task, requiring calibrated models for star formation, feedback from supernovae and AGN, and radiative cooling. Cosmological zoom simulations, in which the region of interest in simulated at a higher resolution than the surrounding region, offer a solution to this problem. This approach has been used on cluster scales (e.g. Martizzi et al. 2014; Hahn et al. 2015); however, it has only been applied to small numbers of clusters to date. This places limitations on the conclusions of such work, since the dynamic range in mass needed to investigate mass-dependent properties is lacking and it is difficult to determine whether any results are significant or an artefact of the small sample size.

To obtain a sample sufficiently large to investigate the properties of massive galaxy clusters, we combine the $400\,h^{-1}$ Mpc BAryons and HAloes of MAssive Systems (BAHAMAS) simulation (McCarthy et al. 2017) with the hydrodynamic zoom simulations

[1] M_Δ is defined as the mass contained within a sphere of radius R_Δ, at which the enclosed average density is Δ times the critical density of the Universe.

Table 1. Cosmological parameters used in the BAHAMAS and MACSIS simulations. All values are consistent with Planck Collaboration XXIV (2016).

Simulation(s)	Ω_m	Ω_b	Ω_Λ	σ_8	n_s	h
BAHAMAS	0.3175	0.04900	0.6825	0.8340	0.9624	0.6711
MACSIS	0.3070	0.04825	0.6930	0.8288	0.9611	0.6777

that were developed as part of the MAssive ClusterS and Intercluster Structures (MACSIS) project (Barnes et al. 2017).

The paper is organized as follows. The simulations used and the methods used to identify haloes and classify relaxed structures are described in Section 2. In Section 3, the methods used to measure the spins, shapes and density profiles of clusters are outlined, and results are presented. This is followed by the results from a WL analysis of the cluster sample in Section 4. In Section 5, we discuss hydrostatic bias in this cluster sample and the method used to calculate the X-ray hydrostatic masses. Finally, we summarize our results in Section 6.

2 SIMULATIONS

2.1 BAHAMAS

The BAHAMAS simulations relevant to this work consist of a DMO simulation (hereafter BAHAMAS-DMO) and a baryonic simulation (hereafter BAHAMAS-HYDRO), which consist of 2×1024^3 particles in boxes with sides of length $400\,h^{-1}$ (comoving) Mpc in the *Planck* cosmology (Planck Collaboration XXIV 2016). The key cosmological parameters are given in Table 1. For the BAHAMAS-HYDRO simulations, the smoothed particle hydrodynamics (SPH) code GADGET-3 (Springel et al. 2005) has been modified to incorporate subgrid prescriptions developed for the OWLS project (Schaye et al. 2010), which model the effects of radiative cooling (Wiersma, Schaye & Smith 2009), star formation (Schaye & Dalla Vecchia 2008) and feedback from AGNs (Booth & Schaye 2009) and supernovae (Dalla Vecchia & Schaye 2008). The calibration of the models for stellar and AGN feedback is described in McCarthy et al. (2017). Briefly, the feedback models (both AGNs and supernovae) were calibrated to reproduce the observed gas fractions of groups and clusters (Vikhlinin et al. 2006; Maughan et al. 2008; Pratt et al. 2009; Sun et al. 2009; Lin et al. 2012) and the global galaxy stellar mass function (Li & White 2009; Baldry et al. 2012; Bernardi et al. 2013).

As shown in McCarthy et al. (2017), the BAHAMAS simulations reproduce both the observed stellar and hot gas properties of groups and clusters, including the observed stellar mass fractions of central galaxies, and the amplitude of the relation between the integrated stellar mass fraction and halo mass for groups and clusters. BAHAMAS also recovers the observed X-ray and Sunyaev–Zel'dovich scaling relations, in addition to their observed pressure and density profiles.

2.2 MACSIS

The MACSIS project is a set of cosmological simulations of massive galaxy clusters described in depth in Barnes et al. (2017).

The foundation of the project is a 3.2 Gpc DMO simulation (hereafter, referred to as the 'parent' simulation), which adopts the *Planck* cosmology (Planck Collaboration XXIV 2016). The large spatial extent of this parent simulation allows for the inclusion of longer wavelength perturbations in the initial conditions, which

Table 2. Mass cuts made to the BAHAMAS (BAH) and MACSIS (MAC) simulations at various redshifts and the number of clusters above various minimum mass limits. Only BAHAMAS clusters with $M_{200} \leq M_{\mathrm{cut}}$ and MACSIS clusters with $M_{200} \geq M_{\mathrm{cut}}$ are included in the cluster sample. N_{cut} is the number of haloes removed in the mass cuts in the MACSIS and BAHAMAS simulations. The outputs of the BAHAMAS and MACSIS simulations at $z \approx 0.25, 0.5$ are at slightly different redshifts. As a consequence, they are not used when looking at any property that may be redshift dependent.

| z | | $M_{\mathrm{cut}}/h^{-1}\,\mathrm{M}_\odot$ | N_{cut} | | $N(M_{200} \geq 5 \times 10^{13}\,h^{-1}\,\mathrm{M}_\odot)$ | | $N(M_{200} \geq 1 \times 10^{14}\,h^{-1}\,\mathrm{M}_\odot)$ | | $N(M_{500} \geq 1 \times 10^{14}\,h^{-1}\,\mathrm{M}_\odot)$ | |
MAC	BAH		MAC	BAH	MAC	BAH	MAC	BAH	MAC	BAH
HYDRO										
0.00	0.00	$10^{14.7}$	59	48	331	3250	331	1192	331	637
0.24	0.25	$10^{14.5}$	46	81	344	2668	344	858	344	397
0.46	0.50	$10^{14.3}$	33	124	357	1956	357	521	355	143
1.00	1.00	$10^{14.1}$	90	86	300	766	300	91	252	1
DMO										
0.00	0.00	$10^{14.7}$	58	48	332	3553	332	1267	332	675
0.24	0.25	$10^{14.5}$	44	72	346	2917	346	923	346	436
0.46	0.50	$10^{14.3}$	30	125	360	2165	360	549	359	170
1.00	1.00	$10^{14.1}$	77	95	313	838	313	95	263	1

leads to the formation of rarer, more massive structures. At $z = 0$, the parent simulation contains more than 100 000 haloes with $M_{200} \geq 10^{14}\,h^{-1}\,\mathrm{M}_\odot$. This simulation has a softening length of $40\,h^{-1}\,\mathrm{kpc}$ at $z = 0$ and a dark matter particle mass of $5.43 \times 10^{10}\,h^{-1}\,\mathrm{M}_\odot$.

A sample of 390 haloes from this parent box were selected for resimulation at higher resolution with the BAHAMAS model. Haloes in the parent simulation were binned by friends-of-friends (FoF) mass in bins of width $\Delta\log_{10}M_{\mathrm{FoF}} = 0.2$ between $10^{15} \leq M_{\mathrm{FoF}}/\mathrm{M}_\odot \leq 10^{16}$. Below $M_{\mathrm{FoF}} = 10^{15.6}\,\mathrm{M}_\odot$, each of these bins was further divided into 10 bins, within which 10 haloes were selected at random to produce a sample of 300 haloes. We have verified that the spins, shapes and concentrations of these haloes are consistent with the underlying parent population. In the parent simulation, there are 90 haloes with masses $M_{\mathrm{FoF}} \geq 10^{15.6}\,\mathrm{M}_\odot$. The most massive halo in the parent box has an FoF mass of $M_{\mathrm{FoF}} = 10^{15.8}\,h^{-1}\,\mathrm{M}_\odot$. All of the most massive 90 haloes were selected for resimulation, producing an overall sample of 390 haloes.

The region around each cluster was resimulated at a higher resolution using the OWLS version of GADGET-3. The resolution of the initial conditions of the parent simulation was progressively degraded with increasing distance from the high-resolution region. This approach includes the large-scale power and tidal forces from the parent box, whilst achieving the desired resolution in the region surrounding the cluster.

Two resimulations were performed for each cluster: one DMO simulation (MACSIS-DMO) with a particle mass of $5.2 \times 10^9\,h^{-1}\,\mathrm{M}_\odot$, and a hydrodynamical simulation (MACSIS-HYDRO). The hydrodynamical simulations used the BAHAMAS code detailed in Section 2.1, with a dark matter particle mass of $4.4 \times 10^9\,h^{-1}\,\mathrm{M}_\odot$ and an initial gas particle mass of $8.0 \times 10^8\,h^{-1}\,\mathrm{M}_\odot$. In the MACSIS and BAHAMAS simulations considered here, the gravitational softening length was set to $4\,h^{-1}\,\mathrm{kpc}$ in physical coordinates for $z \leq 3$ and $16\,h^{-1}\,\mathrm{Mpc}$ in comoving coordinates for $z > 3$.

The BAHAMAS and MACSIS simulations are both consistent with the *Planck* cosmology; however, they use slightly different cosmological parameters, as shown in Table 1. These differences are not important for this study.

As shown in Barnes et al. (2017), the MACSIS simulations reproduce the mass dependence of the observed gas mass, luminosity and integrated Sunyaev–Zel'dovich signal at $z = 0$. They also reproduce the median hot gas profiles of massive galaxy clusters at $z = 0$ and $z = 1$.

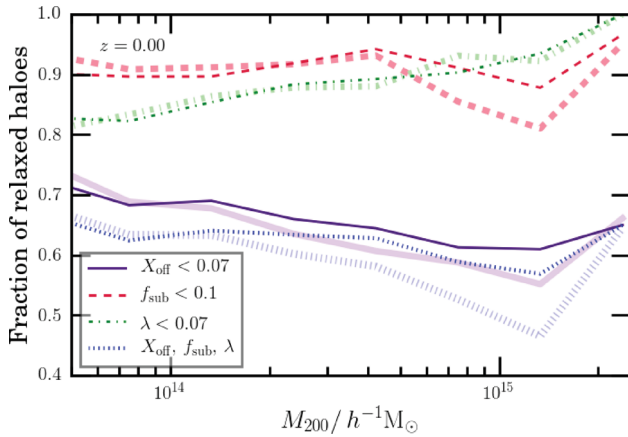### 2.3 Halo definition and selection

Haloes are initially identified using the FoF algorithm with linking length $b = 0.2$ times the mean interparticle separation (Davis et al. 1985). Spherical overdensity masses and radii are determined using the SUBFIND algorithm (Springel et al. 2001), centred on particles with the minimum gravitational potential in the FoF haloes.

Only clusters with $M_{200} \geq 5 \times 10^{13}\,h^{-1}\,\mathrm{M}_\odot$ are included in the sample. At redshift zero, the BAHAMAS-HYDRO simulation has 3298 well-resolved galaxy clusters above this mass cut and all 390 MACSIS clusters (in both the HYDRO and DMO simulations) are above this mass cut. Because of its limited box size, the BAHAMAS simulation has very few high-mass clusters; only nine clusters have masses $M_{200} \geq 10^{15}\,h^{-1}\,\mathrm{M}_\odot$. To ensure the cluster sample is representative, further mass cuts were made to both the BAHAMAS and MACSIS samples. At redshift zero, MACSIS clusters with $M_{200} \leq 10^{14.7}\,h^{-1}\,\mathrm{M}_\odot$ were found to be underconcentrated, with a median spin parameter of 0.034 in the DMO simulations. Conversely, the small fraction of BAHAMAS clusters above this mass cut were found to be overconcentrated, with a median spin parameter of 0.038. For MACSIS, this is a consequence of selecting clusters for resimulation by M_{FoF} rather than M_{200}. For BAHAMAS, this is likely a statistical fluctuation due to the small number of BAHAMAS clusters above this mass cut. These unrepresentative haloes are removed from the sample. Since only a small number of haloes are removed in this mass cut, it does not affect any of the following results. By making a clean cut in both the MACSIS and BAHAMAS simulations, we can easily separate the two sets of simulations when looking at cluster properties versus M_{200}.

Similar mass cuts are made at the other redshifts considered here, with the mass cuts given in Table 2. These mass cuts are used throughout. This table also highlights that the snapshots of the MACSIS and BAHAMAS simulations do not line up perfectly at $z \neq 0, 1$. As a consequence, we only use $z \approx 0.25, 0.5$ when considering redshift-independent properties.

2.4 Relaxation

Since massive galaxy clusters are structures that have collapsed recently, they are dynamic structures which may appear to evolve rapidly. Characterizing such systems is difficult and so we define a relaxed sample of clusters, which are expected to be close to dynamical equilibrium and are less affected by recent merger activity.

Figure 1. The fraction of haloes that are classified as relaxed at $z = 0$ using different relaxation criteria: centre of mass offset (solid line), substructure fraction (dashed), the spin parameter (dot–dashed) and using all three criteria (dotted). The darker colours show the results for the HYDRO simulations and the lighter coloured, thicker lines are for the DMO simulations.

Various criteria have been used in the literature to define relaxed haloes, including the centre of mass offset, X_{off}, the fraction of mass in bound substructures, f_{sub}, the dimensionless spin parameter, λ, and the virial ratio (e.g. Neto et al. 2007; Duffy et al. 2008; Dutton & Macciò 2014; Meneghetti et al. 2014; Klypin et al. 2016). When used in conjunction with other criteria, the virial ratio only removes a small number of haloes (Neto et al. 2007), so we do not use it here. The other parameters are calculated as follows.

(i) The centre of mass offset, X_{off}, is the distance between the minimum of the gravitational potential and the centre of mass of a cluster, divided by the virial radius.[2] The centre of mass is calculated using all particles within the virial radius. Haloes with $X_{off} < 0.07$ are classified as relaxed.

(ii) The substructure fraction, f_{sub}, is the fraction of mass within the virial radius that is bound in substructures. Substructures are only included if they contain more than 100 particles and if their centre is not separated from the cluster centre by more than the virial radius. Haloes with $f_{sub} < 0.1$ are classified as relaxed.

(iii) The spin parameter, λ, is calculated for all particles within R_{200}. We use the alternative expression for the spin parameter from Bullock et al. (2001). Haloes with $\lambda < 0.07$ are classified as relaxed.

The fractions of haloes classified as relaxed according to these criteria are given as a function of mass in Fig. 1, with the darker, thinner (lighter, thicker) lines indicating the results for the DMO (HYDRO) simulations. All three criteria show some mass dependence, with the centre of mass offset and the substructure fraction giving fewer relaxed haloes at high masses. At higher masses, there should be fewer relaxed haloes, since these structures have only formed recently and are likely the result of recent mergers. The spin parameter criterion does not reflect this, since the fraction of haloes classified as relaxed by this criterion increases as a function of mass. This is likely a consequence of the weak mass dependence of the spin parameter (Bett et al. 2007), which is discussed in Section 3.1.

The centre of mass offset criterion removes the largest number of haloes, which is consistent with Neto et al. (2007) and Klypin et al.

---

[2] The virial radius, R_{vir}, is the spherical overdensity mass using $\Delta = \Delta_{vir}$, where Δ_{vir} is calculated using the approximation given in Bryan & Norman (1998).

(2016). Since it is the most stringent criterion, we define relaxed haloes as those where the centre of mass offset $X_{off} < 0.07$, unless stated otherwise.

3 CHARACTERIZING MASSIVE GALAXY CLUSTERS

We use three measures to characterize galaxy clusters: the spin, shape and density profile. The latter is quantified using the concentration parameter.

3.1 Spins

The spin parameter, λ, measures the proportion of energy that is due to the rotation of a cluster. Calculating this parameter requires measuring the total energy of a cluster, which is difficult to define and computationally expensive to compute. Instead, the alternative expression from Bullock et al. (2001) is used to gain an estimate of the spin parameter,

$$\lambda = \frac{J}{\sqrt{2}MV_c R}, \tag{1}$$

where J is the total angular momentum of matter enclosed within a sphere of radius R and mass M, and V_c is the circular velocity at this radius, $V_c = \sqrt{GM/R}$. λ is evaluated at $R = R_{200}$ throughout. For the dark matter component in the HYDRO simulations, the spin parameter is calculated using equation (1) with the total mass of dark matter particles within R_{200}.

The distribution of spins in the DMO simulations is well fitted by a lognormal distribution, in agreement with Bailin & Steinmetz (2005), Bryan et al. (2013) and Baldi et al. (2017) for lower mass haloes. In contrast to Bett et al. (2007), we find no evidence for a longer tail to small values of λ; however, this may be a consequence of the difference in sample size; Bett et al. (2007) considered $>10^6$ haloes. As Table 3 shows, the mean spin parameters are consistent between the DMO and HYDRO simulations. However, the dark matter exhibits a larger mean spin parameter in the HYDRO simulations as compared to the DMO simulations. This is due to a transfer of angular momentum from baryons to the dark matter (Bett et al. 2010; Bryan et al. 2013), which becomes evident by considering the specific angular momentum, $j = J/M$, where J and M are defined in equation (1). The mean specific angular momentum of the dark matter component increases from $\log_{10}(j/h^{-1}\,Mpc^2\,s^{-1}) = 1.50$ in the DMO simulations to $\log_{10}(j/h^{-1}\,Mpc^2\,s^{-1}) = 1.52$ in the HYDRO simulations, which causes an increase in the spin parameter of the dark matter in the HYDRO simulations.

At $z = 0$, selecting only relaxed haloes reduces the mean spin parameter by 15 per cent in both the DMO and HYDRO simulations, which is consistent with Macciò et al. (2007), Jeeson-Daniel et al. (2011) and Bryan et al. (2013).

The mass dependence of spins for the HYDRO simulations is shown in the top panel of Fig. 2, where the markers indicate mean values in mass bins. The lines indicate fits to all individual clusters assuming a relation of the form

$$\log_{10} \lambda = \log_{10} A + B \log_{10}\left(M_{200}/10^{14}\,h^{-1}\,M_\odot\right), \tag{2}$$

where A and B are the best-fitting parameters. Uncertainties on these parameters are obtained by bootstrap resampling the sample 1000 times.

In agreement with the DMO results from Bett et al. (2007) and Muñoz-Cuartas et al. (2011), spin decreases weakly with increasing mass at all redshifts. The slopes at different redshifts are consistent

Table 3. The mean and standard deviation of the halo spin, λ, shape parameters s and e, and concentration c_{200} at $z = 0$ for haloes in the MACSIS and BAHAMAS simulations with $M_{200} \geq 5 \times 10^{13}\ h^{-1}\ \mathrm{M}_{\odot}$. Errors represent 1σ confidence intervals, which are determined by bootstrap resampling the sample 1000 times.

Sample	$\log_{10}\lambda$ Mean	σ	$s = c/a$ Mean	σ	$e = b/a$ Mean	σ	$\log_{10}c_{200}$ Mean	σ
DMO	$-1.446^{+0.006}_{-0.006}$	$0.281^{+0.005}_{-0.005}$	$0.537^{+0.002}_{-0.002}$	$0.107^{+0.002}_{-0.002}$	$0.701^{+0.003}_{-0.003}$	$0.128^{+0.002}_{-0.002}$	$0.642^{+0.003}_{-0.004}$	$0.154^{+0.003}_{-0.003}$
DMO (relaxed)	$-1.515^{+0.007}_{-0.007}$	$0.253^{+0.006}_{-0.005}$	$0.565^{+0.003}_{-0.003}$	$0.097^{+0.002}_{-0.002}$	$0.731^{+0.003}_{-0.003}$	$0.116^{+0.002}_{-0.002}$	$0.700^{+0.003}_{-0.003}$	$0.119^{+0.003}_{-0.003}$
HYDRO	$-1.434^{+0.007}_{-0.006}$	$0.278^{+0.005}_{-0.005}$	$0.576^{+0.002}_{-0.002}$	$0.105^{+0.002}_{-0.002}$	$0.732^{+0.003}_{-0.003}$	$0.123^{+0.002}_{-0.002}$	$0.601^{+0.003}_{-0.003}$	$0.145^{+0.003}_{-0.003}$
HYDRO (relaxed)	$-1.504^{+0.007}_{-0.007}$	$0.251^{+0.006}_{-0.006}$	$0.606^{+0.003}_{-0.003}$	$0.093^{+0.002}_{-0.002}$	$0.761^{+0.003}_{-0.003}$	$0.109^{+0.002}_{-0.002}$	$0.657^{+0.003}_{-0.003}$	$0.109^{+0.004}_{-0.003}$
HYDRO, DM	$-1.410^{+0.007}_{-0.007}$	$0.280^{+0.005}_{-0.005}$	$0.546^{+0.003}_{-0.003}$	$0.109^{+0.002}_{-0.002}$	$0.714^{+0.003}_{-0.003}$	$0.129^{+0.002}_{-0.002}$	$0.621^{+0.003}_{-0.004}$	$0.151^{+0.003}_{-0.003}$
HYDRO, DM (relaxed)	$-1.481^{+0.007}_{-0.007}$	$0.251^{+0.006}_{-0.006}$	$0.575^{+0.003}_{-0.003}$	$0.097^{+0.002}_{-0.002}$	$0.743^{+0.003}_{-0.003}$	$0.116^{+0.002}_{-0.002}$	$0.678^{+0.003}_{-0.003}$	$0.116^{+0.004}_{-0.003}$

within the scatter, yet the normalization decreases with increasing redshift. This is contrary to Muñoz-Cuartas et al. (2011), who found a variable slope for lower mass haloes. This may be a consequence of the difference in mass range considered in the studies. We focus on the high-mass ($>5 \times 10^{13}\ h^{-1}\ \mathrm{M}_{\odot}$) end of the relation, whereas Muñoz-Cuartas et al. (2011) have only a small number of high-mass clusters.

As Table 4 indicates, the normalization of the spin–mass relation is slightly larger in the HYDRO simulations than in the DMO simulations. Considering only relaxed haloes (as determined by X_{off}) reduces the normalization of the λ–M_{200} relation at all redshifts by around 15–20 per cent. The slope of the relation is consistent between the HYDRO and DMO simulations for the full sample. Once only relaxed haloes are selected, we find that the slope is shallower in the DMO simulations.

3.2 Shapes

The shape of a cluster can be characterized by the mass distribution tensor, $\mathcal{M}$, or equivalently the inertia tensor, $\boldsymbol{I}$ (e.g. Bett et al. 2007). In either of these approaches, the cluster is modelled as a uniform ellipsoid with semiprincipal axis lengths $a \geq b \geq c$. The mass distribution tensor of a cluster consisting of N particles is a square matrix with components:

$$\mathcal{M}_{ij} = \sum_{k=1}^{N_{200}} m_k r_{k,i} r_{k,j}, \qquad (3)$$

where m_k is the mass of the kth particle, $r_{k,i}$ is the ith component of the position vector, $\boldsymbol{r}_k$, of the kth particle from the centre of the cluster and the sum is over all particles within R_{200}. The square roots of the eigenvalues of the matrix $\mathcal{M}$ are the lengths of the semiprincipal axes , a, b and c, of the cluster.

The shape of the cluster is parametrized in terms of its sphericity, $s = c/a$, and elongation, $e = b/a$. An idealized spherical structure would have $s = e = 1$. Following Bailin & Steinmetz (2005), we rescale the axis ratios $s \rightarrow s^{\sqrt{3}}$ and $e \rightarrow e^{\sqrt{3}}$ to account for calculating the mass tensor within a spherical region. As discussed in Zemp et al. (2011), Bett (2012) and Bryan et al. (2013), this simple approach is more comparable with observations than other iterative approaches which measure shape within ellipsoidal regions.

The distribution of the sphericity in the DMO simulations at $z = 0$ is well described by a normal distribution with the mean $\langle s \rangle = 0.537$ and standard deviation $\sigma = 0.107$, as given in Table 3. In the HYDRO simulations, the mean sphericity increases to $\langle s \rangle = 0.576$,
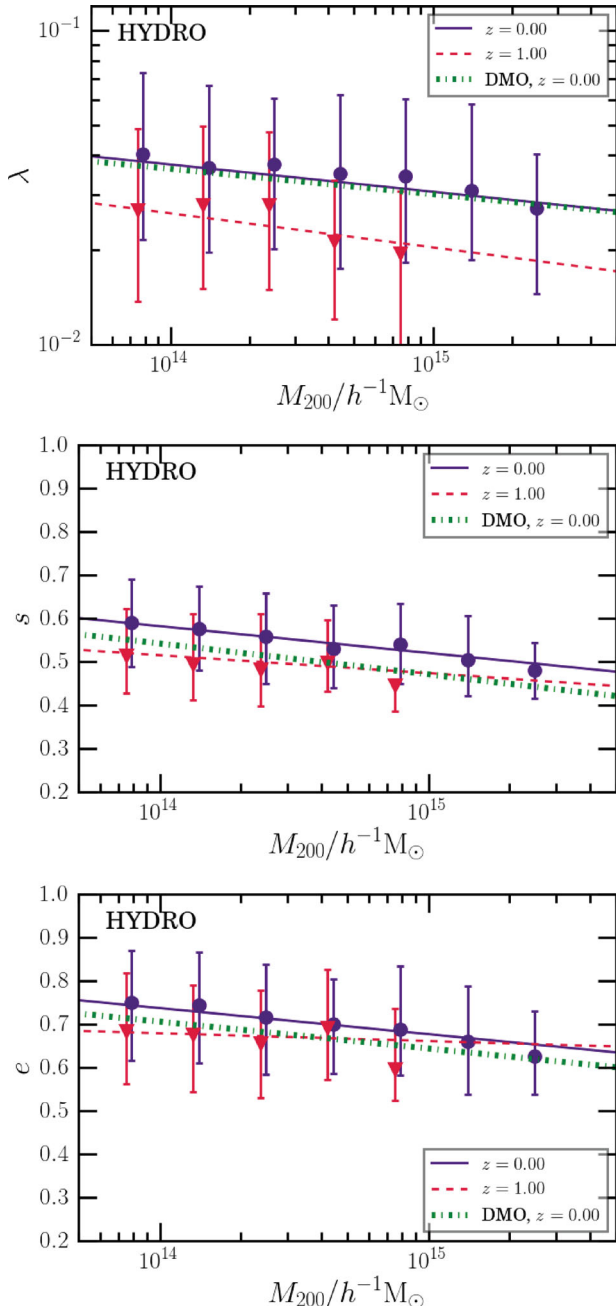
whilst the standard deviation does not change significantly. This increase is predominantly due the increased sphericity of gas in the HYDRO simulations; however, dark matter in the HYDRO simulations is also marginally more spherical than in the DMO simulations, with mean sphericity $\langle s \rangle = 0.546$ in the HYDRO simulations. This difference is also present in the elongation.

Sphericity and elongation as a function of mass for all particles in MACSIS and BAHAMAS clusters in the HYDRO simulations are shown in the middle and bottom panels of Fig. 2. Again, markers indicate median values in mass bins, with error bars showing the 1σ percentiles. The lines indicate best-fitting relations of the form given in equation (2), replacing $\log_{10}\lambda$ for s or e. The general trend of sphericity and elongation decreasing with increasing cluster mass is in agreement with Macciò et al. (2008), Muñoz-Cuartas et al. (2011) and Bryan et al. (2013), indicating that more massive clusters form more extended, aspherical structures. Bryan et al. (2013) consider a number of hydrodynamic models, and find the model most relevant to this work (their AGN simulation) exhibits a steeper mass dependence in the s–M_{200} relation with a slope of -0.078 at $z = 0$. However, in the same work, it is demonstrated that the relation between halo shape and mass is model dependent, with the slope varying from -0.034 to -0.078 at $z = 0$ for different models.

The bottom panel of Fig. 2 shows the elongation ($e = b/a$) as a function of mass for the HYDRO simulations. The mass dependence of the elongation is weaker than for the sphericity, which suggests that as clusters acquire mass, they preferentially collapse along their shortest axis.

As is evident from Table 4, the normalization of the s–M_{200} relation is around 7 per cent higher in the HYDRO simulations compared to the DMO simulations at $z = 0$. Similarly, the normalization of the e–M_{200} relation is ≈ 4 per cent higher in the HYDRO simulations. We find the slope of the s–M_{200} relation to be steeper by ≈ 15 per cent in the DMO simulations at $z = 0$, although the errors on the slopes are ≈ 5–6 per cent, suggesting that a wider mass range is needed to constrain this difference fully. The slopes of the e–M_{200} relations in the HYDRO and DMO simulations are consistent with each other.

Table 4 also gives the s–M_{200} relation for clusters classified as relaxed by X_{off}. Relaxed clusters are more spherical, with a 5 per cent increase in the intercept of the s–M_{200} relation at $z = 0$. The slope of the s–M_{200} relations for relaxed clusters is consistent with that for the full sample. The trends in the e–M_{200} relation mirror this, with a 4 per cent increase in the normalization of the e–M_{200} relation for relaxed haloes and no significant effect on the slope.

Figure 2. The mass dependence of spin, sphericity and elongation in the BAHAMAS-HYDRO and MACSIS-HYDRO simulations at two different redshifts. Markers show the median concentrations in mass bins, with error bars indicating the 16th and 84th percentiles. The lines are fits that are obtained by bootstrap resampling a least-squares fit of equation (2) to individual clusters. The green dot–dashed lines show the best-fitting relations for the DMO simulations at $z = 0$. All three parameters decrease with increasing mass; however, the s–M_{200} and e–M_{200} relations get flatter with increasing redshift, whereas the λ–M_{200} relation steepens with increasing redshift.

Fig. 3 shows the variation of the sphericity with radius for clusters in mass bins in both the HYDRO and DMO simulations. At each radius, the sphericity is calculated using all particles enclosed within a sphere of that radius. In both the HYDRO and DMO simulations, the sphericity of the total matter distribution decreases as a function

of radius, in agreement with the existing work (Hopkins, Bahcall & Bode 2005). Notably, the sphericity profile for the dark matter in the DMO simulations traces the dark matter in the HYDRO simulations in the outer regions. In the central region (considering only radii containing at least 1000 particles), the DMO profiles get shallower in highest mass bin, whilst the dark matter and total matter profiles in the HYDRO simulations do not. As a consequence, clusters in the HYDRO simulations are more spherical in their central regions than DMO clusters, which is likely to be a consequence of the contraction of dark matter in the cluster centres. In the HYDRO simulations, the dark matter dominates the shape of the total matter distribution in the central region, but the contribution of the gas to the total matter distribution becomes significant at $r > 0.2R_{200}$, when the sphericity profiles of the total matter distribution and dark matter distributions start to diverge.

At $r < 0.1R_{200}$ in the lowest mass bin, the sphericity profiles in the DMO and the HYDRO simulations seem to reconverge; however, a higher resolution study is needed to confirm this since the clusters in this study have an insufficient number of particles for their shape measurements to be well converged there. For the same reason, we cannot comment on the shape of the stellar mass distribution in this study.

3.3 Density profiles and concentrations

3.3.1 The impact of baryons on cluster profiles

Density profiles are obtained for clusters by binning particles in 50 equally spaced logarithmic bins in the range $10^{-2} \leq r/R_{vir} \leq 1$. Fig. 4 shows the mean density profiles for clusters in the HYDRO simulations stacked in mass bins. At all radii considered here, the total matter density profile (red triangles) is dominated by the dark matter component (purple circles). Considering only the baryonic component, stars (black crosses) dominate in the inner region of lower mass clusters, with gas dominating outside of that region. The radius at which stars begin to dominate is neither constant nor a fixed fraction of R_{200}. For the most massive clusters ($M_{200} \geq 10^{15} \, h^{-1} \, M_{\odot}$), the gas component dominates over the stellar component at all plotted radii. The shapes of the mean stellar and gas density profiles are consistent with the shapes of mean profiles for haloes with masses greater than $10^{13} \, h^{-1} \, M_{\odot}$ in Schaller et al. (2015).

Since the MACSIS sample consists of 390 individual clusters that have been simulated both as DMO and HYDRO clusters, they are ideal for studying the impact of baryons on the dark matter profile. The top panel of Fig. 5 shows the mean fractional difference between the total matter density profiles in the DMO and HYDRO simulations at $z = 0$, where clusters have been individually matched. We see that the density profiles are more concentrated in the HYDRO simulations, with an increase in the density profile at small radii and a decrease at $r \approx R_{200}$ compared to the DMO simulations. This difference is not simply due to the baryonic component condensing at the cluster centre; it is also present in the dark matter distribution, as can be seen from the bottom panel of Fig. 5. Since all the clusters considered in this figure have masses $M_{200} \geq 10^{14.7} \, h^{-1} \, M_{\odot}$, our results show the impact of baryons on the density profiles of clusters in this mass range. However, this is consistent with previous works looking at less massive structures that have found that the inclusion of baryonic effects leads to a contraction of the inner halo, causing an increase in the dark matter profile at small radii (e.g. Duffy et al. 2010; Schaller et al. 2015).

Table 4. Best-fitting slope and intercept parameters for the mass dependence of halo spin, λ, shape parameters, s and e, and concentration, c_{200}, assuming the parameters (as they are listed in the table) are linearly related to $\log_{10}(M_{200}/10^{14}\,h^{-1}\,\mathrm{M_\odot})$. For all but c_{200}, the fits are performed for haloes with $M_{200} \geq 5 \times 10^{13}\,h^{-1}\,\mathrm{M_\odot}$. For c_{200}, only haloes with $M_{200} \geq 10^{14}\,h^{-1}\,\mathrm{M_\odot}$ are used to ensure that the density profiles are converged over the radial range $0.05 \leq r/R_{\rm vir} \leq 1$. Errors represent 1σ confidence intervals, which are determined by bootstrap resampling the sample 1000 times.

	$\log_{10}\lambda$		$s = c/a$		$e = b/a$		$\log_{10}c_{200}$	
	Intercept	Slope	Intercept	Slope	Intercept	Slope	Intercept	Slope
$z = 0$								
DMO	$0.0362^{+0.0004}_{-0.0004}$	$-0.0810^{+0.0120}_{-0.0120}$	$0.541^{+0.002}_{-0.002}$	$-0.071^{+0.004}_{-0.004}$	$0.705^{+0.002}_{-0.002}$	$-0.062^{+0.005}_{-0.005}$	$4.511^{+0.057}_{-0.055}$	$-0.138^{+0.010}_{-0.009}$
DMO (relaxed)	$0.0307^{+0.0003}_{-0.0003}$	$-0.0432^{+0.0134}_{-0.0136}$	$0.568^{+0.002}_{-0.002}$	$-0.076^{+0.005}_{-0.005}$	$0.733^{+0.002}_{-0.002}$	$-0.071^{+0.006}_{-0.007}$	$5.195^{+0.058}_{-0.057}$	$-0.149^{+0.010}_{-0.010}$
HYDRO	$0.0374^{+0.0004}_{-0.0004}$	$-0.0873^{+0.0117}_{-0.0113}$	$0.581^{+0.002}_{-0.002}$	$-0.062^{+0.004}_{-0.004}$	$0.736^{+0.002}_{-0.002}$	$-0.060^{+0.005}_{-0.005}$	$4.068^{+0.048}_{-0.047}$	$-0.073^{+0.009}_{-0.009}$
HYDRO (relaxed)	$0.0316^{+0.0004}_{-0.0004}$	$-0.0695^{+0.0131}_{-0.0130}$	$0.610^{+0.002}_{-0.002}$	$-0.067^{+0.004}_{-0.004}$	$0.765^{+0.002}_{-0.002}$	$-0.068^{+0.006}_{-0.006}$	$4.626^{+0.104}_{-0.108}$	$-0.074^{+0.008}_{-0.008}$
$z = 1$								
DMO	$0.0260^{+0.0005}_{-0.0005}$	$-0.0772^{+0.0269}_{-0.0274}$	$0.472^{+0.003}_{-0.003}$	$-0.046^{+0.010}_{-0.010}$	$0.651^{+0.004}_{-0.004}$	$-0.016^{+0.013}_{-0.013}$	–	–
DMO (relaxed)	$0.0206^{+0.0005}_{-0.0005}$	$-0.0542^{+0.0343}_{-0.0369}$	$0.496^{+0.004}_{-0.004}$	$-0.055^{+0.014}_{-0.014}$	$0.671^{+0.005}_{-0.005}$	$-0.021^{+0.017}_{-0.018}$	–	–
HYDRO	$0.0261^{+0.0005}_{-0.0005}$	$-0.1085^{+0.0276}_{-0.0277}$	$0.513^{+0.003}_{-0.003}$	$-0.042^{+0.010}_{-0.010}$	$0.678^{+0.004}_{-0.004}$	$-0.019^{+0.013}_{-0.013}$	–	–
HYDRO (relaxed)	$0.0210^{+0.0005}_{-0.0005}$	$-0.0680^{+0.0339}_{-0.0343}$	$0.541^{+0.004}_{-0.004}$	$-0.054^{+0.013}_{-0.013}$	$0.700^{+0.005}_{-0.005}$	$-0.028^{+0.016}_{-0.017}$	–	–

3.3.2 Navarro—Frenk—White or Einasto?

The density profiles of dark matter haloes are commonly fitted by the two-parameter Navarro—Frenk—White (NFW) model, proposed by Navarro, Frenk & White (1997):

$$\rho_{\rm NFW}(r) = \frac{\rho_{\rm crit}\delta_{\rm c}}{(r/r_{-2})(1 + r/r_{-2})^2}, \qquad (4)$$

which is characterized by an overdensity, $\delta_{\rm c}$ and a scale radius, r_{-2}. The scale radius is the radius at which the density profile has an isothermal slope. However, numerous authors have found that haloes have a steeper than NFW slope at small radii (Moore et al. 1998; Jing & Suto 2000; Fukushige & Makino 2001), whilst others have found a shallower slope (Navarro et al. 2004; Merritt et al. 2006), which suggests that a model with a variable inner slope may be more appropriate. Gao et al. (2008), Dutton & Macciò (2014) and Klypin et al. (2016) have found that dark matter density profiles more closely follow the Einasto profile (Einasto 1965):

$$\rho(r) = \delta_{\rm c}\rho_{\rm crit} \exp\left\{ -\frac{2}{\alpha}\left[\left(\frac{r}{r_{-2}}\right)^\alpha - 1\right]\right\}, \qquad (5)$$

which has a logarithmic slope parametrized by α.

For clusters with $M_{200} \geq 10^{14}\,h^{-1}\,\mathrm{M_\odot}$, best-fitting cluster profiles are obtained by fitting profiles in the radial range $0.05 \leq r/R_{\rm vir} \leq 1$. This mass cut is made to ensure that the convergence radius (calculated following Power et al. 2003) is always within the inner fitting radius. The model profile parameters are adjusted to minimize

$$\rho_{\rm rms} = \frac{1}{N_{\rm dof}}\sum_i^{N_{\rm bins}}\left[\log_{10}\rho_i - \log_{10}\rho_{\rm model}(\boldsymbol{p})\right]^2, \qquad (6)$$

where $N_{\rm dof}$ is the number of degrees of freedom (e.g. $N_{\rm dof} = N_{\rm bins} - 2$ for the NFW profile), ρ_i is the density in radial bin i and $\boldsymbol{p}$ is the vector of parameters: $\boldsymbol{p} = (r_{-2}, \delta_{\rm c})$ for an NFW profile and $\boldsymbol{p} = (r_{-2}, \delta_{\rm c}, \alpha)$ for an Einasto profile.

The top panel of Fig. 6 shows the goodness of fit (defined in equation 6) for NFW and Einasto fits to clusters in the HYDRO simulations. For the NFW profile, the goodness of fit is, on average, larger, with median($\rho_{\rm rms}$) = 0.047 ± 0.001 as compared to 0.040 ± 0.001 for the Einasto model, which indicates that the NFW model is a slightly poorer fit to cluster profiles than the Einasto model. The goodness of fit for the NFW profile also exhibits a larger scatter.

These results are echoed in the DMO simulations (not shown) with median($\rho_{\rm rms}$) = 0.048 ± 0.001 for the NFW model and 0.041 ± 0.001 for the Einasto model.

The bottom panel of Fig. 6 shows mass estimates obtained from fits to spherically averaged density profiles in the HYDRO simulations. Both the NFW and Einasto models slightly underpredict cluster masses, with median($M_{200,\rm model}/M_{200}$) = $0.968^{+0.002}_{-0.001}$ and $0.992^{+0.001}_{-0.001}$ for the NFW and Einasto models, respectively. A similar difference is present in the DMO simulations, in which median($M_{200,\rm model}/M_{200}$) = $0.976^{+0.002}_{-0.002}$ for the NFW model and $0.992^{+0.001}_{-0.002}$ for the Einasto model. The slight improvement of the Einasto model in reproducing cluster masses over the NFW model is a consequence of the better fit the Einasto model provides to cluster mass profiles.
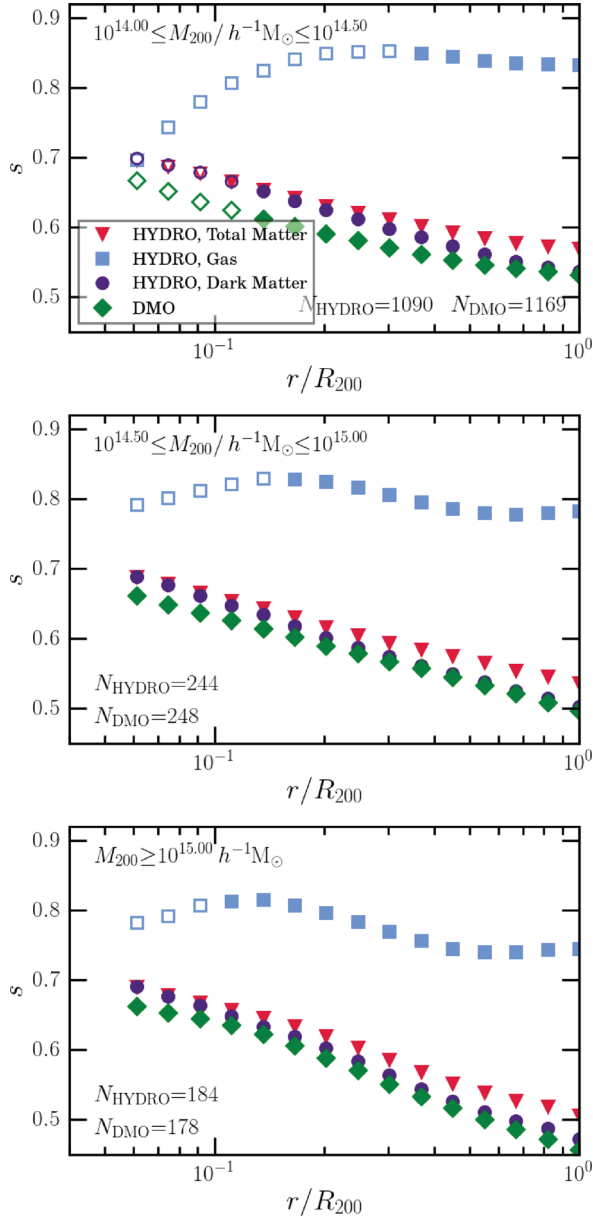
3.3.3 The concentration–mass relation

Fig. 7 shows concentration as a function of mass for the total matter distribution in relaxed clusters in the DMO and HYDRO simulations. Concentrations are obtained by fitting two-parameter NFW profiles. The relationship between concentration and mass is well fitted by a power law,

$$c_{200} = A\left(\frac{M_{200}}{10^{14}\,h^{-1}\,\mathrm{M_\odot}}\right)^B, \qquad (7)$$
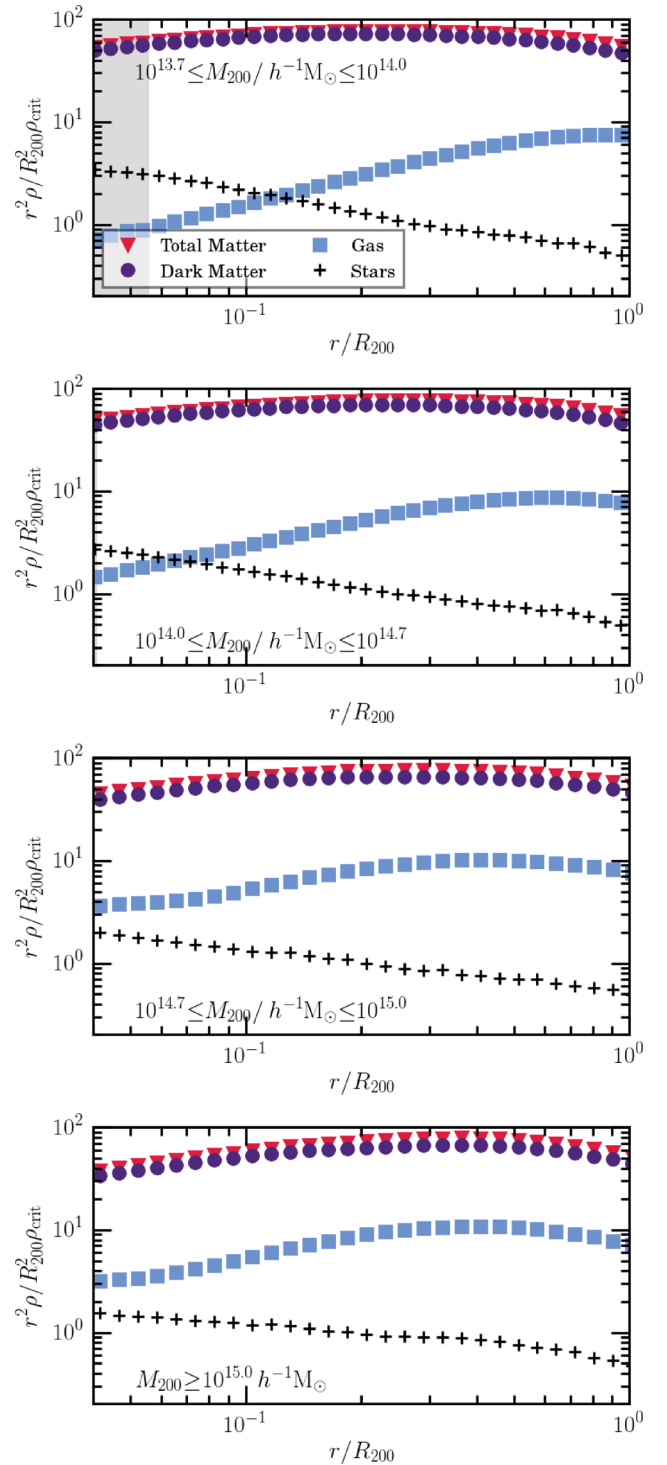
so that in Fig. 7, B is the slope. The best-fitting parameters are given in Table 4, with the uncertainties on the fit parameters obtained through bootstrap resampling the fit 1000 times. The best-fitting concentration–mass relation for the DMO simulation exhibits a steeper slope than that found in literature (Neto et al. 2007; Duffy et al. 2008; Dutton & Macciò 2014); however, Fig. 7 illustrates that the data are consistent with the results of Dutton & Macciò (2014), who use the *Planck* cosmology. The difference between the concentration–mass relation presented here and that found in wider literature is not surprising since this analysis is limited only to large masses ($M_{200} \geq 10^{14}\,h^{-1}\,\mathrm{M_\odot}$), which have not been extensively studied in other works.

In summary, low-mass clusters in the HYDRO simulations are more spherical and more centrally concentrated than their DMO counterparts. This is a consequence of both the condensation of baryons in the cluster centre and the contraction of the dark matter
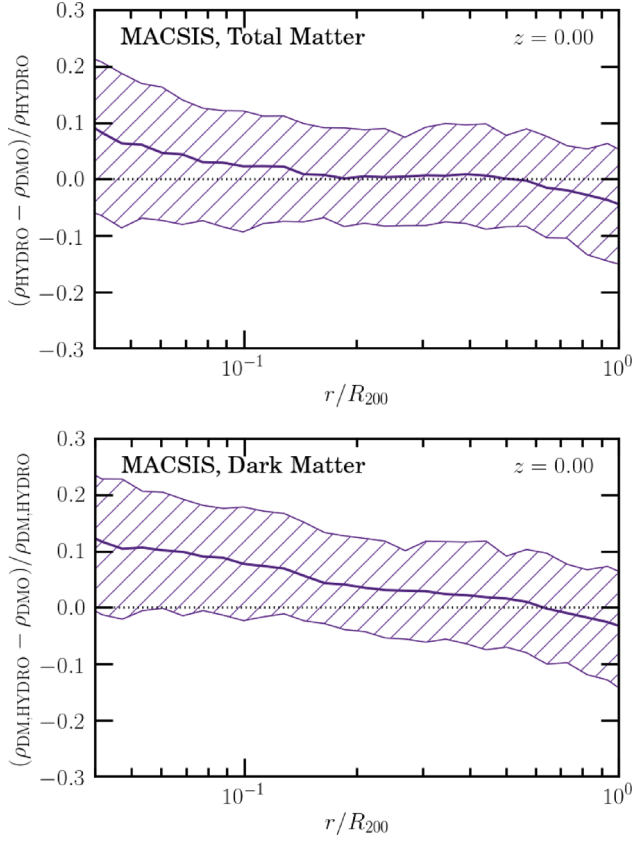
Figure 3. The sphericity as a function of radius in mass bins for clusters in the BAHAMAS and MACSIS simulations at $z = 0$. The red triangles, light blue squares and purple circles indicate the shapes of the total matter, gas and dark matter distributions in the HYDRO simulations. The green diamonds are for the DMO simulations. Filled markers indicate radii at which the enclosed number of particles is greater than 1000 in each cluster in the bin. Similar trends are apparent in all mass bins. At $r > 0.2R_{200}$, the shapes of total matter and dark matter distributions in the HYDRO simulations start to diverge as gas starts to contribute significantly. The sphericity profile in the outer regions of the DMO simulations traces the dark matter in the HYDRO simulations, rather than the total matter distribution.

Figure 4. The mean density profiles for the gas (blue squares), stars (black crosses), dark matter (purple circles) and total matter (red triangles) for clusters stacked by cluster mass at $z = 0$. The top two panels show profiles for clusters in the BAHAMAS-HYDRO simulation and the bottom two panels show profiles of clusters in the MACSIS-HYDRO simulations. The shaded grey region indicates the largest convergence radius in each mass bin. From top to bottom, each bin contains 2058 (0), 1335 (0), 0 (142) and 0 (189) BAHAMAS (MACSIS) clusters, respectively.

halo in the presence of baryons. It is more significant in high-mass clusters, which leads to a flatter concentration–mass relation in the HYDRO simulations. The density profiles of clusters in both the HYDRO and DMO simulations are well fitted by the NFW profile; however, the Einasto model provides a marginally better fit and gives less biased mass estimates.

Figure 5. In the top panel, the solid purple line is the median fractional difference in the total matter density profiles of matched clusters in the DMO and HYDRO MACSIS simulations at $z = 0$. These clusters span the mass range $10^{14.7} \leq M_{200}/h^{-1}\,\mathrm{M}_\odot \leq 10^{15.6}$. The hatched purple region shows the 16th to 84th percentiles. The bottom panel shows the fractional difference in the dark matter density profiles for matched haloes, where the dark matter density profile in the DMO simulations has been rescaled by the factor of $\Omega_{\mathrm{DM}}/\Omega_{\mathrm{m}}$, where Ω_{DM} is the dark matter fraction and Ω_{m} is the total matter fraction.

4 CLUSTER WEAK LENSING

The use of galaxy clusters as cosmological probes requires well-constrained galaxy cluster masses. Cluster WL, which measures the statistical distortion of background galaxies due to the mass of the intervening cluster, is touted as a largely unbiased technique for measuring cluster masses. Furthermore, the shear profiles of galaxy clusters are also used to test ΛCDM and theories of modified gravity (e.g. Okabe et al. 2013; Wilcox et al. 2015). The shear profiles and WL mass estimates of galaxy clusters have been studied extensively in DMO simulations (Becker & Kravtsov 2011; Bahé et al. 2012); however, the impact of baryons on the projected mass distribution is not so well understood.

WL studies measure the shape distortion of background galaxies, which is quantified in the reduced shear,

$$g = \frac{\gamma}{1-\kappa}, \tag{8}$$

in which γ is the shear and κ is the convergence. The shear describes the tidal gravitational force and has two components, $\gamma = \gamma_1 + i\gamma_2$. The convergence describes the isotropic focusing of light and is proportional to the projected surface density of the lens, Σ,

$$\kappa = \frac{\Sigma}{\Sigma_{\mathrm{crit}}}, \tag{9}$$

Figure 6. The top panel shows the goodness-of-fit for NFW (purple, diagonal hatching) and Einasto (pink, dotted hatching) fits to clusters in the HYDRO simulations with $M_{200} \geq 10^{14}\,h^{-1}\,\mathrm{M}_\odot$ at $z = 0$. The arrows indicate median values for the NFW (purple) and Einasto (pink) models, respectively. The bottom panel shows the mass inferred from the best-fitting NFW and Einasto profiles. Einasto profiles provide a better fit to the density profiles of clusters and, on average, provide better estimates of cluster masses.

where $\Sigma(R)$ is the integral of the 3D density profile along the line of sight,

$$\Sigma(R) = 2 \int_0^\infty \rho(r = \sqrt{R^2 + z^2})\mathrm{d}z, \tag{10}$$

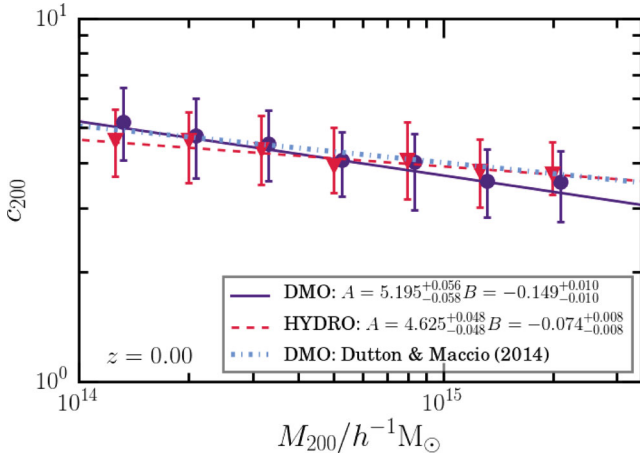and Σ_{crit} is the critical surface density,

$$\Sigma_{\mathrm{crit}} \equiv \frac{1}{4\pi G} \frac{D_{\mathrm{s}}}{D_{\mathrm{d}} D_{\mathrm{ds}}}, \tag{11}$$

where D_{s}, D_{d} and D_{ds} are the angular distances between the observer and source galaxies, observer and lens, and lens and source galaxies, respectively (e.g. Wright & Brainerd 2000). We ignore the effect of shape noise, which is noise due to averaging over a finite number of source galaxies within each pixel.

WL studies of clusters probe only shape distortions tangential to the line from the projected cluster centre. The tangential component of the shear is

$$\gamma_{\mathrm{t}} = \mathrm{Re}\left[\gamma e^{-2i\phi}\right], \tag{12}$$

where ϕ is the polar angle of the cluster (e.g. Bartelmann & Schneider 2001).

Figure 7. The mass dependence of cluster concentration for the total matter distribution in relaxed BAHAMAS- and MACSIS-HYDRO (red triangles) and DMO (purple circles) clusters at two different redshifts. Concentrations are obtained by fitting NFW profiles to the total matter density profiles of clusters over the radial range $0.05 \leq r/R_{vir} \leq 1$. Markers show the median concentrations in mass bins, with error bars indicating the 16th to 84th percentiles. The lines are fits that are obtained by bootstrap resampling a least-squares fit of equation (7) to individual clusters. The concentration–mass relation from Dutton & Macciò (2014) is shown in light blue. DMO clusters have higher concentrations at low masses and exhibit a stronger mass dependence.

4.1 Weak lensing shear and X-ray surface brightness maps

Surface density maps are produced for each cluster in the BAHAMAS and MACSIS simulations by selecting all particles within a radius of $5R_{200}$ of the cluster centre and projecting these along the desired line of sight. Reducing the selection region to within a radius of $3R_{200}$ of the cluster centre does not affect the results presented here; however, reducing this radius further changes the results. Particles are then smoothed to a 2D grid with a cell width of $10 \, h^{-1}$ kpc using SPH smoothing with 48 neighbours. Gas, stars and dark matter are smoothed separately, and the resulting maps are summed to give a total matter mass map. Three orthogonal projections were taken of each cluster, one along each axis of the simulation box.

Convergence maps are obtained by dividing surface density maps by Σ_{crit}. The shear is related to the convergence through their Fourier transforms (e.g. Schneider et al. 2006):

$$\tilde{\gamma} = \left(\frac{\hat{k}_x^2 - \hat{k}_y^2}{\hat{k}_x^2 + \hat{k}_y^2} + i \, \frac{2\hat{k}_x \hat{k}_y}{\hat{k}_x^2 + \hat{k}_y^2} \right) \tilde{\kappa}, \tag{13}$$

where $\tilde{\gamma}$ and $\tilde{\kappa}$ are the Fourier transforms of the shear and convergence, respectively, and $\hat{k}_x$ and $\hat{k}_y$ are wavenumbers. The source redshift is taken to be $z = 1$ throughout this work.

We also compute X-ray surface brightness maps to compare the gas and total matter distributions. These are produced as follows. The X-ray luminosity for each particle is obtained using the cooling function calculated using the Astrophysical Plasma Emission Code (APEC; Smith et al. 2001) with updated atomic data and calculations from the ATOMDB v2.0.2 (Foster et al. 2012). We use the element abundances that are tracked in the simulation (H, He, C, N, O, Ne, Mg, Si, S, Ca and Fe). The X-ray surface brightness is calculated from the luminosity by dividing through the angular area of each pixel. The distribution of particle luminosities within $5R_{200}$ is then projected along one axis and smoothed using SPH smoothing to give

a 2D map of the X-ray emission. Further details of this approach are given in Barnes et al. (2017).

Fig. 8 shows the shear field (tick marks) of four MACSIS clusters at $z = 0.24$, with X-ray surface brightness in the background. The top left-hand image in Fig. 8 is of a dynamically relaxed cluster with mass $M_{200} = 1 \times 10^{15} \, h^{-1} \, M_{\odot}$, with a roughly symmetrical shear field and only one X-ray peak. In contrast, the image on the top right is of a merger with $M_{200} = 2 \times 10^{15} \, h^{-1} \, M_{\odot}$, which shows how the presence of substructure disturbs the shear field. The bottom two images are two orthogonal projections of the same $M_{200} = 1.5 \times 10^{15} \, h^{-1} \, M_{\odot}$ cluster. Considering only the emission within R_{200}, the X-ray emission of the YZ (right-hand panel) projection appears relatively relaxed and the shear field is roughly symmetrical. However, in the XY projection (left), we see multiple X-ray peaks and a perturbed shear field, illustrating how one cluster can look drastically different in different projections.

4.2 Weak lensing profiles and mass estimates

In observations, galaxy cluster masses are obtained from a reduced tangential shear map by first calculating a shear profile and then fitting it with a model profile, from which a mass can be inferred. We obtain reduced tangential shear profiles for each cluster by finding the mean reduced shear in 20 logarithmically spaced bins in the range $0.1 \leq r/h^{-1}$ Mpc ≤ 3. Both the NFW and Einasto models assume spherical symmetry. For an axisymmetric halo, the radial dependence of the tangential shear is (e.g. Wright & Brainerd 2000)

$$\gamma(r) = \frac{\bar{\Sigma}(<r) - \Sigma(r)}{\Sigma_{crit}}, \tag{14}$$

where $\bar{\Sigma}(<r)$ is the mean surface mass density of the halo within a radius r,

$$\bar{\Sigma}(<r) = \frac{2}{r^2} \int_0^r x \Sigma(x) \mathrm{d}x. \tag{15}$$

To obtain the shear of an NFW halo, equation (15) is numerically integrated using the analytic form for $\Sigma(r)$ from Bahé et al. (2012). This is then substituted into equation (14). A similar process is used for Einasto profiles; however, in the absence of an analytic form for $\Sigma(r)$ using a truncated line of sight, equation (10) is numerically integrated to obtain $\Sigma(r)$ for an Einasto halo.
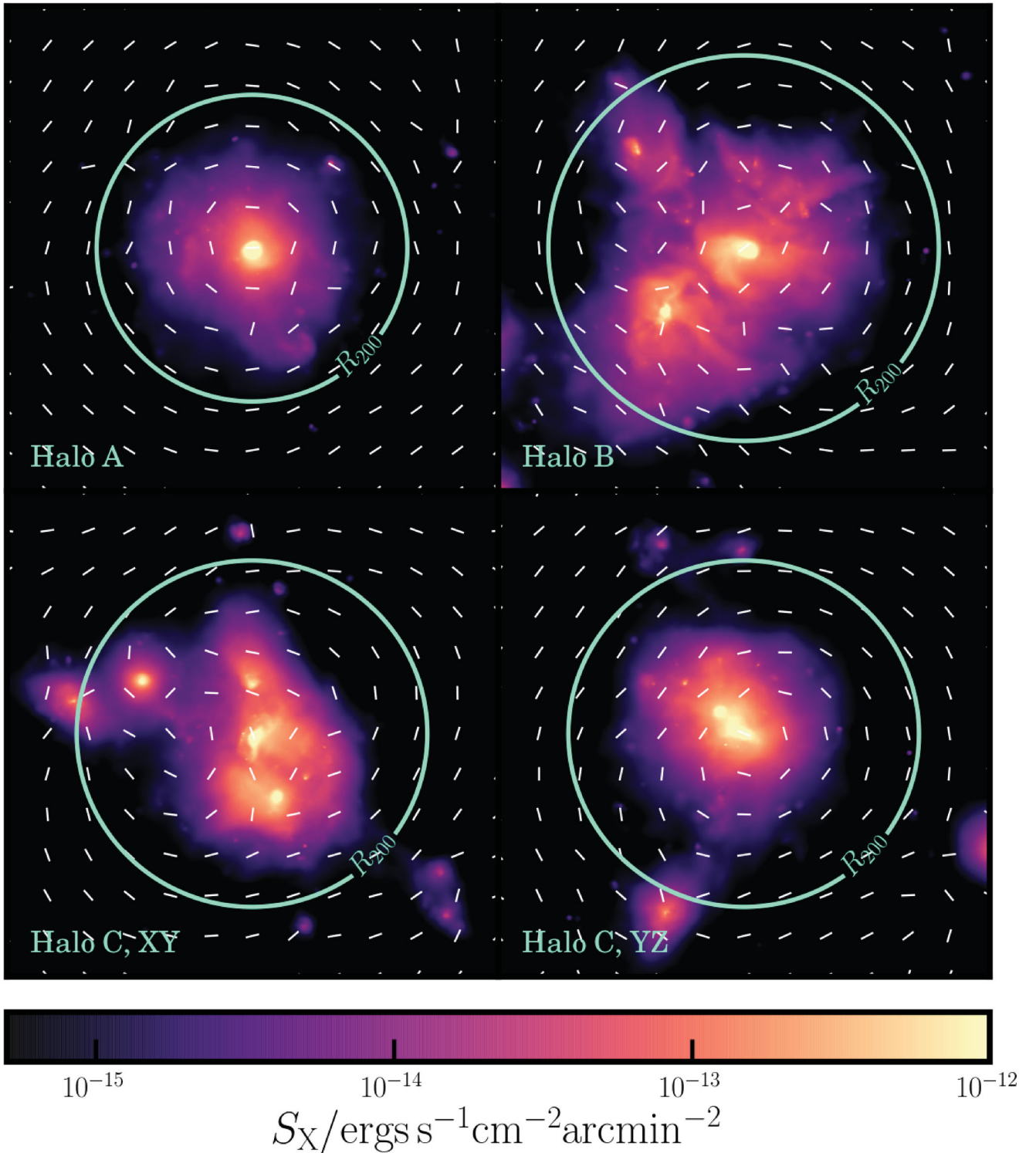
The best-fitting model is found by minimizing

$$g_{rms} = \frac{1}{N_{dof}} \sum_i^{N_{bins}} \left[\log_{10} g_{T,i} - \log_{10} g_{T,model}(r, \boldsymbol{p}) \right]^2, \tag{16}$$

where N_{dof} is the number of degrees of freedom, $g_{T,i}$ is the reduced tangential shear measured in the ith shell and $\boldsymbol{p}$ is the vector of fit parameters; $\boldsymbol{p} = (r_s, \delta_c)$ for an NFW profile and $\boldsymbol{p} = (r_s, \delta_c, \alpha)$ for an Einasto profile. Given the best-fitting parameters for a particular model, an estimate of R_{200} is obtained by solving the equation

$$\int_0^{R_{200,WL}} \rho(r, \boldsymbol{p}) r^2 \mathrm{d}r = \frac{200}{3} \rho_{crit}(z) R_{200,WL}^2 \tag{17}$$

for $R_{200,WL}$. The cluster mass estimate, $M_{200,WL}$, is then given by

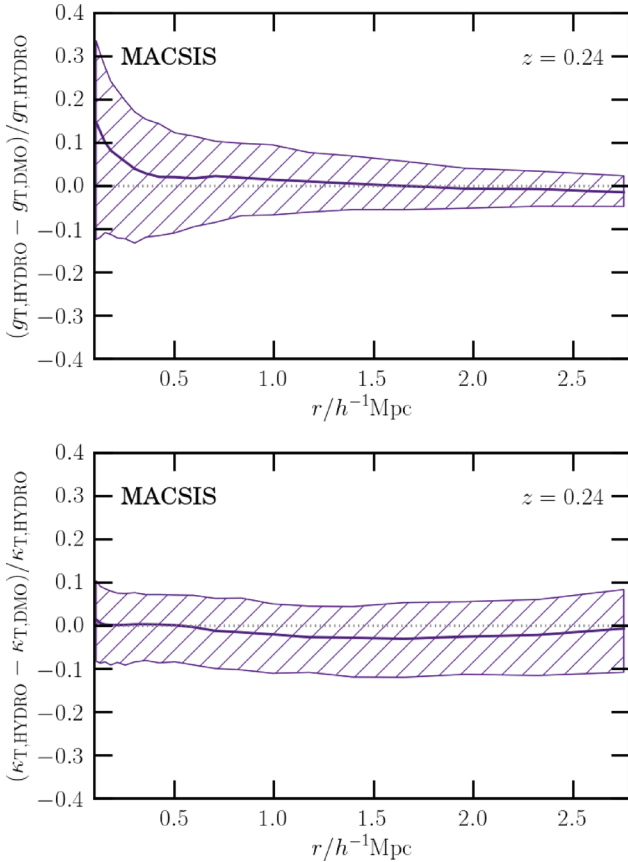$$M_{200,WL} = \frac{4\pi}{3} 200 \rho_{crit}(z) R_{200,WL}^3. \tag{18}$$

Figure 8. The X-ray surface brightness, S_X of four MACSIS clusters at $z = 0.24$ with quivers representing the WL shear field. Each image is centred on the minimum gravitational potential for the cluster and is $6 \times 6 \, h^{-1}$ Mpc across, with a projection depth of $10 \, R_{200}$. The MACSIS sample contains a wide range of relaxed (e.g. the top left cluster) and unrelaxed clusters (top right). The bottom two images show two orthogonal projections of the same cluster. In the image on the bottom left, the cluster appears to be extended with multiple X-ray peaks, which may lead to it being classed as morphologically unrelaxed in observations. In contrast, the image on the bottom right, whilst still containing multiple X-ray peaks, is more spherically symmetric.

Fig. 9 shows the median fractional difference between the reduced shear profiles of matched clusters in the MACSIS-DMO and -HYDRO simulations. Since all the clusters considered in this figure have masses $M_{200} \geq 10^{14.5} \, h^{-1} \, M_{\odot}$, our results show the impact of

baryons on the shear profiles of clusters in this mass range. The shear is 12–15 per cent larger in the central regions ($r < 150 \, h^{-1}$ kpc) of clusters in HYDRO simulations as compared to DMO simulations. This is not caused by the projection of the mass distribution, since
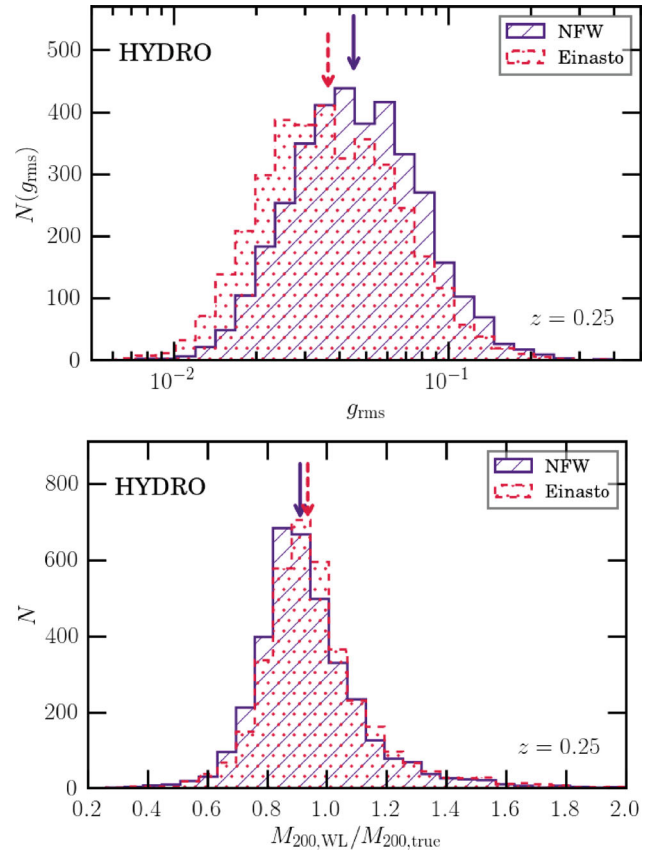
Figure 9. In the top panel, the solid purple line is the median fractional difference in the reduced tangential shear profiles, $g_T(r)$, of matched clusters in the DMO- and HYDRO-MACSIS simulations at $z = 0.24$. The hatched purple region shows the 16th and 84th percentiles. The bottom panel shows the fractional difference in the convergence profiles of matched haloes at the same redshift. Baryons have a stronger impact in the central regions of the reduced shear profile than is apparent in the convergence profile.
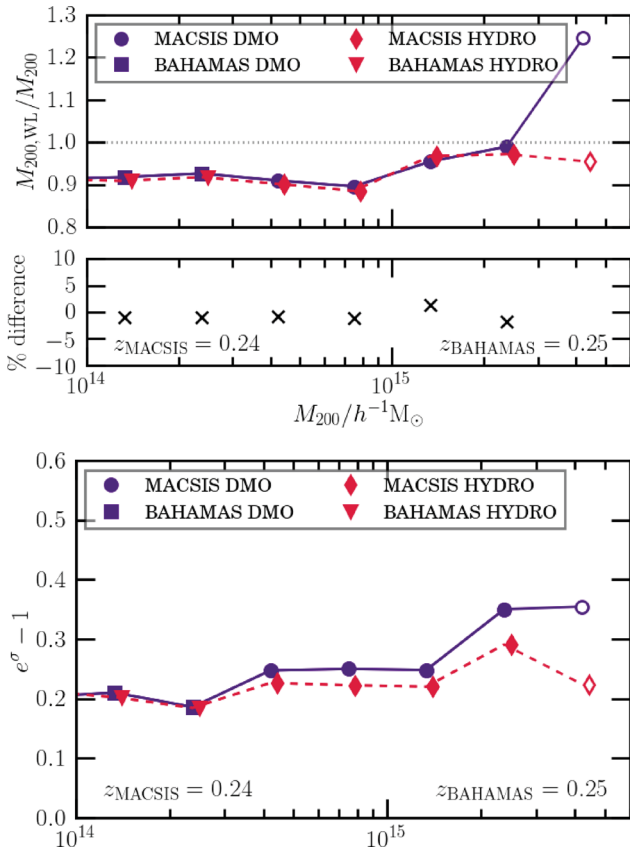

Figure 10. The top panel shows the goodness of fit for the best-fitting NFW (purple, diagonal hatching) and Einasto (pink, dotted hatching) profiles to the reduced tangential shear profiles of clusters in the HYDRO simulations with $M_{200} \geq 10^{14} \, h^{-1} \, M_\odot$ at $z = 0.25$. The bottom panel shows masses inferred from these fits in units of the true mass. As in 3D, Einasto profiles provide a better fit to the density profiles of clusters and, on average, provide slightly better estimates of cluster masses.

the fractional difference in the convergence profile (bottom panel of Fig. 9) does not show this increase in the central region. Instead, this reflects the sensitivity of the shear to the central cluster region. This is highlighted in equation (14), which gives the shear profile for an axisymmetric halo. Since the clusters are more centrally concentrated in the HYDRO simulations, this increases in $\bar{\Sigma}(<r)$ in the HYDRO simulations. At $r > 0.5 \, h^{-1}$ Mpc, clusters in the HYDRO simulations are less dense than their DMO counterparts (see the bottom panel of Fig. 9), which means that $\bar{\Sigma}(<r)$ then tends to the DMO value as r increases. Even outside the central region, the shear profile is sensitive to the behaviour at the centre, which makes it a more sensitive probe of baryonic effects than the convergence.

At larger radii ($r > 1 \, h^{-1} \, M_\odot$), the shear profiles from HYDRO and DMO simulations agree to within 5 per cent. There is significant scatter around the median values, with some clusters showing no difference between HYDRO and DMO clusters in the inner regions.

The top panel of Fig. 10 shows that when fitting the reduced tangential shear profiles of clusters, the NFW model provides an adequate fit, with a median residual $g_{\mathrm{rms}} = 0.0453^{+0.0004}_{-0.0007}$. However, the Einasto model gives a markedly better fit, with median $g_{\mathrm{rms}} = 0.0365^{+0.0004}_{-0.0003}$. This improved fit results in a slightly better mass estimate, as shown in the bottom panel of Fig. 10. Considering all BAHAMAS and MACSIS clusters at $z = 0.25$, the median ratio of the estimated mass to the true mass for the

Einasto model is $M_{200,\mathrm{WL}}/M_{200} = 0.936^{+0.003}_{-0.002}$, as compared to $M_{200,\mathrm{WL}}/M_{200} = 0.911^{+0.002}_{-0.003}$ for the NFW model. However, given the difficulty in obtaining observational data of sufficient quality to constrain a three-parameter fit, the minor decrease in the bias when using the Einasto model is hard to justify.

Despite the impact of baryons on the central regions of galaxy clusters, including baryons has only a marginal impact on the WL mass reconstruction at R_{200}. This is illustrated in Fig. 11, in which the top panel shows the median ratio of the WL mass to the true mass, $M_{200,\mathrm{WL}}/M_{200}$, as a function of true mass. The results from the DMO and HYDRO simulations agree to within 5 per cent in all but the last mass bin, which contains only nine projections (three clusters). This figure shows the masses inferred from fitting with an NFW profile. Fitting with an Einasto model still gives median ratios that are consistent between the HYDRO and DMO simulations. Consistent with existing work (Becker & Kravtsov 2011; Oguri & Hamana 2011; Bahé et al. 2012), the bias ($b_{\mathrm{WL}} = 1 - M_{200,\mathrm{WL}}/M_{200}$) decreases with increasing mass for $M_{200} \geq 10^{15} \, h^{-1} \, M_\odot$ when using either the NFW or the Einasto model.

We find a larger bias in our WL mass estimates (in both DMO and HYDRO) compared with that found in Becker & Kravtsov (2011) and Bahé et al. (2012); however, our results are broadly consistent with Oguri & Hamana (2011). This discrepancy is more pronounced at masses $M_{200} \approx 10^{14} \, h^{-1} \, M_\odot$, where Bahé et al. (2012) find a

Figure 11. The top panel shows the median ratio of the WL mass to the true mass in mass bins obtained by fitting NFW profiles to reduced tangential shear maps for the DMO (purple solid line) and HYDRO (pink dashed line) simulations as a function of mass. Circles and diamonds (squares and triangles) are used to indicate results from the MACSIS (BAHAMAS) simulations. Markers are offset horizontally for clarity. The unfilled markers represent bins containing fewer than 10 projections. The percentage difference between the DMO and HYDRO results is shown in the middle panel. The bottom panel shows the scatter in the bias as a function of mass, where σ is the standard deviation.

bias of $b_{\rm WL} \sim 5$ per cent compared to our $b_{\rm WL} \sim 9$ per cent. There are numerous differences between their analysis and that presented here: notably, the method for fitting NFW profiles and the resolution of the underlying simulations. We fit NFW profiles to azimuthally averaged shear profiles, whereas Bahé et al. (2012) fit directly to background ellipticities. The simulations used here have a dark matter particle mass of $5.2 \times 10^9 \, h^{-1} \, {\rm M_\odot}$, which is roughly an order of magnitude larger than the particle mass in the Millennium Simulations used by Bahé et al. (2012). We also ignore the effect of shape noise, which has been shown to reduce the bias in WL mass estimates by ~ 2 per cent (Bahé et al. 2012). These differences are expected to affect both the HYDRO and DMO simulations equally, which means that they do not affect our main conclusion: including baryons has no significant effect upon the bias in WL mass estimates. Note, however, that baryons do change the true mass, M_{200}, and that studies comparing with DMO mass predictions will still obtain biased results.

Since the bias is lognormally distributed, the scatter around these points is $e^\sigma - 1$, where σ is the standard deviation of the distribution of the bias in mass bins. This is presented in the bottom panel of the same figure. At masses greater than $4 \times 10^{14} \, h^{-1} \, {\rm M_\odot}$, a difference in the scatter in DMO and HYDRO simulations emerges. Whilst

the scatter is dominated by the alignment of the cluster with the line of sight (in agreement with Bahé et al. 2012), this difference is likely due to substructures. For $M_{200} \geq 10^{14} \, h^{-1} \, {\rm M_\odot}$ at $z = 0.25$, HYDRO clusters have smaller values of $f_{\rm sub}$, on average, than their DMO counterparts.

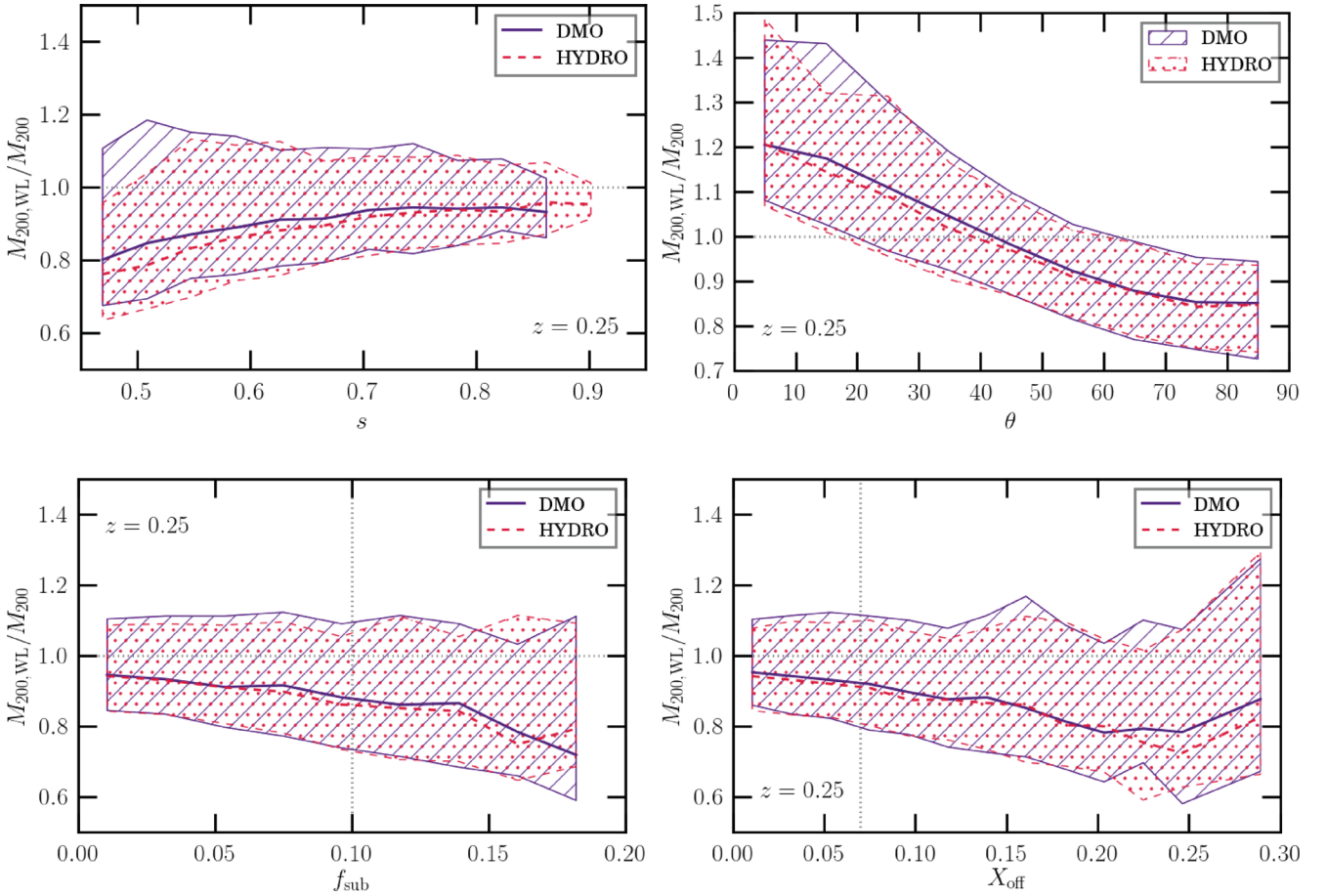### 4.3 The correlation of weak lensing mass bias with cluster parameters

Fig. 12 shows the dependence of the bias in WL mass estimates on sphericity, alignment, the substructure fraction and the centre of mass offset. Since $M_{200,\,\rm WL}/M_{200}$ tends to unity with increasing mass, and sphericity decreases with increasing mass, the increase of $M_{200,\,\rm WL}/M_{200}$ with increasing sphericity is not simply a by-product of the mass dependence of the sphericity. The top left-hand image in Fig. 12 shows that there is also an offset between the DMO and HYDRO simulations when plotting against sphericity. This offset is also present in the top right-hand image in the same figure, which shows the mass bias as a function of the alignment of the cluster, θ, where θ is the angle between the longest semiprincipal axis of the cluster and the line of sight. For $\theta < 43°$ ($\theta > 43°$), the masses of clusters that are elongated along the line of sight are, on average, overestimated (underestimated).

The bottom panels of Fig. 12 show the dependence of the WL mass bias on two parameters typically used to characterize the dynamical state of clusters in simulations: the substructure fraction and the centre of mass offset. The more the substructure in a cluster, the greater the bias in its WL mass. A similar trend is present for $X_{\rm off}$, with the masses of clusters exhibiting a large centre of mass offset being underestimated by around 20 per cent. There appears to be an upturn at $X_{\rm off} > 0.25$ in both the DMO and HYDRO simulations, with the last bin consisting of 12 (15) projections in the DMO (HYDRO) simulations. From a visual inspection of the projected mass distributions of these clusters, this appears to be a consequence of substructures appearing to be in the central cluster regions due to projection effects. Whilst this only occurs in one projection per cluster, in these cases it has led to such a large overestimate of the mass that the median bias is higher than at smaller values of $X_{\rm off}$.

5 HYDROSTATIC BIAS

Cluster WL is only one method for estimating cluster masses. Another widely used approach is to calculate masses from the gas temperature and density profiles derived from X-ray observations. This approach assumes that clusters are in hydrostatic equilibrium, which may lead to a bias in the resulting masses. This hydrostatic mass bias has been studied thoroughly in the literature, yet a consistent narrative is yet to emerge. The bias is typically parametrized in terms of $b_{\rm X} = 1 - M_{\rm X}/M_{\rm WL}$, where $M_{\rm X}$ is the hydrostatic mass obtained from a cluster's X-ray emission.

For observations, Applegate et al. (2014), Israel et al. (2014) and Smith et al. (2016) find a bias of only $b_{\rm X} = 0.04, 0.08$ and 0.05, respectively. Yet this is at odds with results from von der Linden et al. (2014b), Hoekstra et al. (2015) and Simet et al. (2015), who find $b_{\rm X} = 0.30, 0.24$ and 0.22, respectively. The hydrostatic bias has been shown to be larger at larger radii (Zhang et al. 2010), which may go some way to explaining the result from Applegate et al. (2014), where it is measured at R_{2500}. However, the results from Israel et al. (2014) and Smith et al. (2016) are measured at R_{500}. It should also be noted that these studies use different X-ray data sets; for example Applegate et al. (2014) use a sample of 12 relaxed clusters, whereas von der Linden et al. (2014b) use a

Figure 12. The dependence of the ratio of the WL mass to the true mass, $M_{200,\,WL}/M_{200}$, on cluster sphericity, s, alignment, θ, substructure fraction, f_{sub}, and centre of mass offset, X_{off}, at $z = 0.25$ for both the DMO (purple, diagonal hatching) and HYDRO (pink, dotted hatching) simulations. The solid lines indicate median values and the hatching represents the 1σ percentiles. Vertical dashed lines in the bottom panels indicate thresholds used to define relaxed clusters. For alignment, $\theta = 90°$ indicates a cluster with its principal axis perpendicular to the line of sight and $\theta = 0°$ indicates a cluster with its principal axis parallel to the line of sight.

subset of clusters from the *Planck* catalogue (Planck Collaboration XXIX 2014) that are also present in the Weighing the Giants sample (von der Linden et al. 2014a). Since these studies span overlapping mass ranges, mass can also not account for the disparity. Smith et al. (2016) attribute the difference to redshift, suggesting that the bias at $z > 0.3$ may be larger as a consequence of observational systematics.
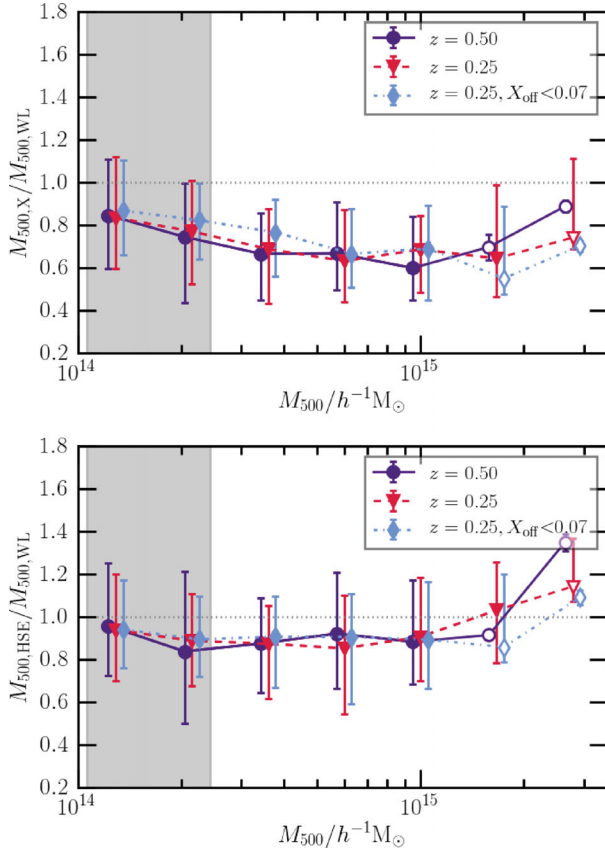
Yet this would not explain the contrast between the results of Applegate et al. (2014), Israel et al. (2014) and Smith et al. (2016), and the results from numerical simulations. Numerical simulations have typically found a bias of ~20 per cent for groups and clusters (Nagai, Vikhlinin & Kravtsov 2007; Kay et al. 2012; Rasia et al. 2012; Le Brun et al. 2014), with some dependence on the implementation of baryonic physics (Kay et al. 2012; Le Brun et al. 2014). Since simulating massive clusters with hydrodynamics (including realistic feedback) is computationally expensive, most of these works have not had sufficient numbers of high-mass clusters to characterize the mass dependence of the hydrostatic bias. Combining the MACSIS and BAHAMAS samples gives a large sample of clusters spanning $10^{14} \leq M_{500}/h^{-1}\,M_\odot \leq 10^{15}$.

To obtain hydrostatic masses for clusters in the BAHAMAS and MACSIS simulations, the X-ray spectra of all particles within $5R_{200}$ are calculated and then binned into 25 radial bins spaced logarithmically between $0.03R_{200}$ and $5R_{200}$. As described in Le Brun et al.

(2014), gas particles with temperature $k_B T < 10^{5.2}$ keV and number density $n \geq 0.1\,cm^{-3}$ are excluded. Modifying the threshold of these cuts by up to an order of magnitude or excluding bound substructures has no meaningful effect on our results. In each radial bin, the emission spectrum is fitted with a single temperature APEC model, giving a temperature, T_X, density, ρ_X, and metallicity. We find assuming a fixed metallicity leads to a larger bias in the measured temperatures, so we fit for the temperature, density and metallicity simultaneously. We fit the spectra in the range of 0.05–10.0 keV and extending this range to 0.05–20.0 keV does not affect our results. We fit the density and temperature profiles using the functional forms in Vikhlinin et al. (2006). Under the assumption of hydrostatic equilibrium, these are used to infer a mass profile and thus a mass.

Fig. 13 shows the ratio of the X-ray hydrostatic mass to the mass inferred from WL, $1 - b = M_{500,\,X}/M_{500,\,WL}$, as a function of true mass, M_{500}. WL masses and hydrostatic masses are calculated independently. WL masses are calculated using the approach described in Section 4.2, replacing 200 for 500 in equations (17) and (18). Our findings for $M_{200,\,WL}/M_{200}$ are consistent with those for $M_{500,\,WL}/M_{500}$.

In the top panel of Fig. 13, which shows hydrostatic masses obtained from spectroscopic temperature and density profiles, we see that the hydrostatic mass is consistently smaller than the WL mass
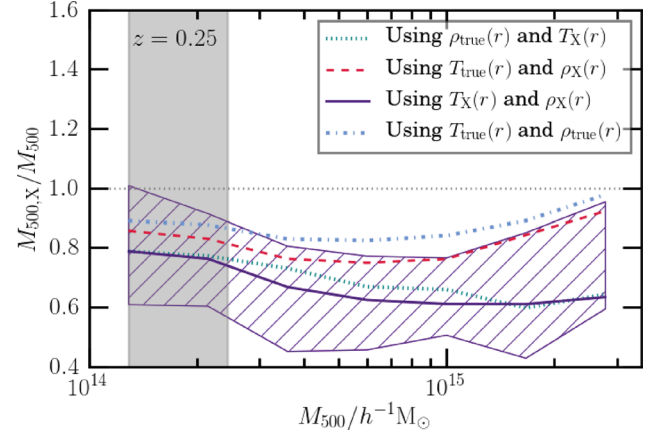
Figure 14. The ratio of X-ray mass to true mass when using the mass-weighted temperature, $T_{\text{true}}(r)$, profile and the true gas density profile, $\rho_{\text{true}}(r)$ (line blue dot–dashed line), as compared to the bias when using the X-ray temperature profile, $T_{\text{X}}(r)$, and the X-ray density profile, $\rho_{\text{true}}(r)$ (solid purple line). The hatched region shows the scatter in the bias obtained when using X-ray observables. The shaded grey region shows the mass range where the MACSIS and BAHAMAS simulations overlap. Masses obtained from X-ray observables are consistently lower, with the X-ray temperature providing the largest contribution (some percentage here) to the mass bias.

Figure 13. The dependence of the ratio of the X-ray hydrostatic mass to the mass inferred from WL, $M_{500,\,\text{X}}/M_{500,\,\text{WL}}$, on the true mass of the cluster at $z = 0.25, 0.5$. The top panel shows hydrostatic masses derived using spectroscopic temperatures and densities. The bottom panel shows hydrostatic masses derived using true temperatures and densities. WL masses and hydrostatic masses are calculated independently. The shaded grey region shows the mass range where the MACSIS and BAHAMAS simulations overlap. Excluding the highest mass bin (which contains fewer than 10 clusters), the ratio decreases as a function of mass when using spectroscopic values. The mass bias is independent of redshift. Selecting relaxed clusters (clusters with $X_{\text{off}} < 0.07$) has no significant effect on the bias. WL masses were obtained by taking one random projection of each cluster. The markers are offset horizontally for clarity.

for clusters of all masses. The bias increases from $b_{\text{X}} = 0.2$ to 0.35 as the mass increases from 10^{14} to $10^{15}\,h^{-1}\,\text{M}_{\odot}$. There appears to be an upturn at $M_{500} \geq 10^{15}\,h^{-1}\,\text{M}_{\odot}$; however, since the highest mass bin contains only nine projections (three clusters), this may be a consequence of limited statistics. There is no evidence for any redshift dependence. As the light blue dot–dashed line shows, selecting relaxed clusters does not reduce the bias. We have confirmed that the spectra and functional forms for the density and temperature profiles are well fitted.

Whilst the bias in X-ray mass measurements is referred to as the hydrostatic bias, it does not only reflect the bias due to the assumption that the cluster is hydrostatic. As the bottom panel of Fig. 13 shows, if a hydrostatic mass is calculated using the true density and temperature profiles, $\rho_{\text{true}}(r)$ and $T_{\text{true}}(r)$, then the bias is significantly reduced to $b_{\text{X}} = 0.04$–0.14 for all bins containing at least 10 clusters. This difference is independent of redshift and is still present when considering only relaxed haloes.

Fig. 14 shows that the bias in the X-ray temperature profile is the dominant contribution to the mass bias, since using the density
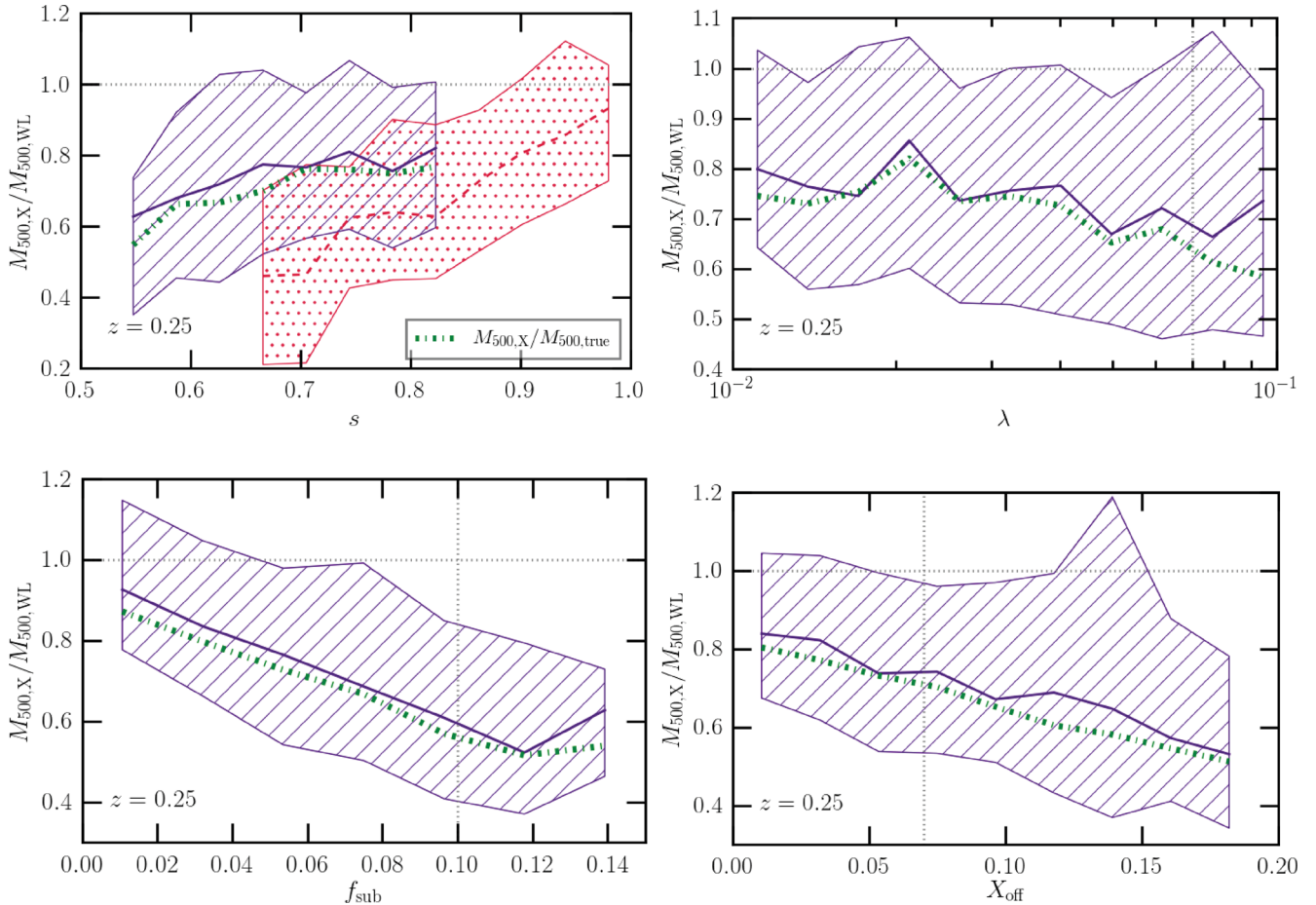
profile derived from X-ray observations has very little effect. This is consistent with the work of Rasia et al. (2012) and Biffi et al. (2016). Rasia et al. (2012) noted that the temperature inhomogeneities in the intracluster medium lead to lower X-ray temperatures, which, in turn, leads to smaller X-ray masses. They suggested that including feedback from AGNs would reduce this effect; however, it is clearly still present in both these simulations and those studied in Biffi et al. (2016). We have extensively tested our analysis pipeline and find that the lower X-ray temperatures are a consequence of cooler gas (with $T \sim 1$–3 keV) emitting X-rays in the cluster outskirts. Since excluding gas in substructures does not affect our results, we can infer that this gas is not bound in substructures. Further work is needed to investigate the origin of this gas; it may be gas that is stripped from infalling substructures or it may be cool accreted gas. Since these simulations use a traditional SPH scheme, which has been shown to lead to a lack of mixing in the simulations (Sembolini et al. 2016a), it is possible that the presence of this cool gas may be an unphysical artefact that arises from a lack of mixing in the intracluster medium. However, Sembolini et al. (2016b) found that the differences in cluster cores due to the hydrodynamics solver are overwhelmed by differences due to the inclusion of AGN feedback and differences in its implementation. Furthermore, it is not yet clear what amount of mixing is realistic, since it may depend on other effects not considered here (e.g. the magnetic field structure of the intracluster medium).

If we consider the hydrostatic mass calculated using $\rho_{\text{true}}(r)$ and $T_{\text{true}}(r)$ (rather than the gas density and temperature profiles as obtained from mock X-ray observations) to be representative of the hydrostatic bias, then we find $M_{500,\,\text{X}}/M_{500,\,\text{true}} \approx 0.8$–$0.9$ for clusters in the mass range $10^{14} \leq M_{500}/h^{-1}\,\text{M}_{\odot} \leq 3 \times 10^{15}$.

Finally, in Fig. 15 we show the dependence of the ratio of the X-ray hydrostatic mass (calculated using spectral temperatures and densities) to the mass inferred from WL as a function of sphericity, spin, substructure fraction and centre of mass offset. The bias shows a strong dependence on sphericity, with a smaller bias for more spherical clusters. For sphericity, the purple line indicates

Figure 15. The dependence of the ratio of the X-ray hydrostatic mass to the mass inferred from WL, $M_{500,\mathrm{X}}/M_{500,\mathrm{WL}}$, on cluster sphericity, s, spin, λ, substructure fraction, f_{sub}, and X_{off} at $z = 0.25$ for the HYDRO simulations. The green dot–dashed line shows the dependence of the ratio of the X-ray hydrostatic mass to the true mass, $M_{200,\mathrm{X}}/M_{200,\mathrm{true}}$, on the same parameters. The thick solid lines indicate median values in mass bins and the hatched regions indicate 1σ percentiles. The hydrostatic bias is measured for the total mass distribution and the purple solid lines indicate parameters measured for the total mass distribution. The pink dashed line in the top left-hand panel indicates the sphericity of the gas distribution only. The sphericity and spin parameter are measured within R_{200}. The substructure fraction and centre of mass offset are measured within the virial radius. The hydrostatic mass bias shows a stronger dependence on the sphericity of the gas than on the sphericity of the total matter distribution. WL masses and hydrostatic masses are calculated independently. Vertical dashed lines indicate thresholds used to define relaxed clusters.

the hydrostatic bias against the sphericity of the total mass distribution, whereas the pink line is the bias against the sphericity of the gas. The hydrostatic bias exhibits a tighter correlation and a stronger mass dependence with gas sphericity than with the total matter sphericity. This is not driven by the WL mass estimate, since the same trend is present in $M_{500,\mathrm{X}}/M_{\mathrm{true}}$ (the green dot–dashed line). Instead, this justifies the morphological selections used in X-ray observations (Postman et al. 2012), since it suggests that clusters that are more spherical will exhibit a smaller hydrostatic mass bias.

Despite the frequent use of spin as an indicator of the dynamical state of a cluster in simulations (e.g. Klypin et al. 2016), we find that the hydrostatic bias is largely independent of spin, regardless of the approach used to calculate the hydrostatic mass. Rather, it shows a strong dependence on the substructure fraction, with higher values of f_{sub} yielding a larger bias. This dependence persists even when cool dense clumps are not removed from the cluster prior to calculating hydrostatic masses. Since we find that X-ray masses are less biased for clusters that are more spherical and contain less substructure, this suggests that the bias is lower for older clusters, which have accreted less material recently.

If the substructure fraction reflects the appearance of multiple peaks in the X-ray emission, then this motivates the X-ray selection techniques based on a visual identification of the substructure (e.g. Nurgaliev et al. 2013; Rasia, Meneghetti & Ettori 2013). We defer a more detailed study of the former assumption to later work. Finally, the hydrostatic bias also correlates with the centre of mass offset. Yet, the large scatter in these relations demonstrates that even the hydrostatic masses of clusters with small values of f_{sub} and X_{off} can be biased low by up to 20 per cent.

6 SUMMARY

In this study, we have used the MACSIS and BAHAMAS simulations presented in Barnes et al. (2017) and McCarthy et al. (2017) to create a combined sample of more than 3500 clusters with $M_{200} \geq 5 \times 10^{13}\,h^{-1}\,\mathrm{M_\odot}$, simulated with realistic baryonic physics. These simulations have been shown to reproduce the observed scalings of gas mass, integrated Sunyaev–Z'eldovich signal and X-ray luminosity with mass, as well as the observed hot gas radial profiles of clusters at $z = 0$ (Barnes et al. 2017; McCarthy et al. 2017).

We focus our study on three key areas: the properties of high-mass clusters and the impact of baryons upon them, the influence of baryonic effects upon WL mass estimates and the mass dependence of the hydrostatic bias in high-mass clusters.

Since the MACSIS simulations consist of matched HYDRO and DMO zoom simulations, we are able to directly compare clusters simulated with and without baryonic effects. We also investigated the redshift dependence of our results. Our main results are as follows:

(i) The distributions of spins in the HYDRO and DMO simulations are consistent with each other and are well fitted by a lognormal distribution. The dark matter component has a slightly larger spin in the HYDRO simulations than in the DMO simulations, which is associated with a transfer in angular momentum from the baryonic component to the dark matter. Spin declines weakly with mass at all redshifts considered here (Fig. 2). The slope is consistent between the HYDRO and DMO simulations and is unchanged for a relaxed subsample. The mean spin of relaxed haloes is 15 per cent smaller than for the entire cluster sample.

(ii) Clusters in the HYDRO simulations are more spherical, with larger values of s and e on average. The sphericity–mass relation is steeper in the DMO simulations, but the elongation–mass relation is consistent between the DMO and HYDRO simulations. A larger mass range is required to constrain the effect of baryons on this slope. Selecting only relaxed haloes does not affect the slope of either the sphericity–mass or the elongation–mass relation.

(iii) By matching MACSIS clusters in the DMO and HYDRO simulations, we demonstrated that clusters in the HYDRO simulations are more concentrated in the central regions (Fig. 5). This is partly due to the condensation of baryons in the cluster centre and also a consequence of the contraction of the dark matter halo in the presence of baryons. The dark matter density profiles of MACSIS clusters at $z = 0$ in the HYDRO simulations are more dense at $r < 0.6R_{200}$ than in the DMO simulations. At $0.6 < r/R_{200} < 3$, the dark matter density profile is less dense in the HYDRO simulations than in the DMO simulations. At the high-mass end of the concentration–mass relation ($M_{200} > 10^{15} \, h^{-1} \, \mathrm{M_\odot}$), this manifests itself as an increase in concentrations in the HYDRO simulations (Fig. 7). Since the concentration–mass relation is flatter in the HYDRO simulations, clusters with masses $M_{200} \approx 10^{15} \, h^{-1} \, \mathrm{M_\odot}$ have larger concentrations than clusters in the DMO simulations.

(iv) The density profiles of clusters considered here are better fitted by the Einasto profile than the NFW profile. This leads to a smaller bias in the masses calculated from fits to the spherically averaged density profile, with the NFW model underpredicting masses by 22 per cent on average and the Einasto model underpredicting masses by 8 per cent (Fig. 6). Whilst cluster shear profiles are better fitted by the Einasto model rather than the NFW model, this only results in a 2–3 per cent improvement in WL cluster mass estimates in the HYDRO simulations, despite the cost of adding an additional degree of freedom (Fig. 10).

(v) Baryons have a more significant effect on the shear profiles of clusters than on their convergence profiles. The shear profiles of HYDRO clusters are up to 15 per cent larger than clusters in the DMO simulations at $r < 0.5 \, h^{-1} \, \mathrm{M_\odot}$, as a consequence of the sensitivity of the shear to the central cluster region (Fig. 9). Despite this, the WL mass bias is consistent between the DMO and HYDRO simulations, with both data sets showing that WL underestimates cluster masses by ≈ 10 per cent for clusters with $M_{200} \leq 10^{15} \, h^{-1} \, \mathrm{M_\odot}$ and that this bias tends to zero at higher masses (Fig. 11).

(vi) The hydrostatic mass bias, $1 - b = M_{500,\mathrm{X-ray}}/M_{500,\mathrm{WL}}$, declines from 0.8 to 0.6 for clusters with masses increasing from $M_{500} = 10^{14}$ to $10^{15} \, h^{-1} \, \mathrm{M_\odot}$ when using X-ray hydrostatic masses calculated from spectroscopic temperature and density profiles (Fig. 13). The X-ray and WL masses are measured independently. We find no evidence for any redshift dependence. The mass dependence is mostly due to the spectroscopic temperature measurements (Fig. 14) that are biased low by the presence of cooler, X-ray emitting gas in the cluster outskirts. Using the true temperature and density profiles gives $b \approx 0.04$–0.14 at the masses considered here, with no clear mass dependence.

(vii) The hydrostatic bias is smaller for more spherical clusters that have a small centre of mass offset and fewer substructures, which motivates the morphological selection of clusters in X-ray surveys (Fig. 15).

In conclusion, we find baryons have only a minor effect on the spins, shapes and WL mass estimates of massive galaxy clusters. Baryons have a small effect on cluster density profiles at small radii, which is also apparent in their WL shear profiles. When using spectroscopic temperatures and densities, the hydrostatic bias decreases as a function of mass, leading to a bias of ≈ 40 per cent for high-mass clusters. Further work is needed to clarify the cause of this large bias and to reconcile it with observational results.

REFERENCES

Allen S. W., Evrard A. E., Mantz A. B., 2011, ARA&A, 49, 409
Applegate D. E. et al., 2014, MNRAS, 439, 48
Bahé Y. M., McCarthy I. G., King L. J., 2012, MNRAS, 421, 1073
Bailin J., Steinmetz M., 2005, ApJ, 627, 647
Baldi A. S., De Petris M., Sembolini F., Yepes G., Lamagna L., Rasia E., 2017, MNRAS, 465, 2584
Baldry I. K. et al., 2012, MNRAS, 421, 621
Barnes D. J., Kay S. T., Henson M. A., McCarthy I. G., Schaye J., Jenkins A., 2017, MNRAS, 465, 213
Bartelmann M., Schneider P., 2001, Phys. Rep., 340, 291
Becker M. R., Kravtsov A. V., 2011, ApJ, 740, 25
Benson B. A. et al., 2014, Proc SPIE, 9153, 91531P
Bernardi M., Meert A., Sheth R. K., Vikram V., Huertas-Company M., Mei S., Shankar F., 2013, MNRAS, 436, 697
Bett P., 2012, MNRAS, 420, 3303
Bett P., Eke V., Frenk C. S., Jenkins A., Helly J., Navarro J., 2007, MNRAS, 376, 215
Bett P., Eke V., Frenk C. S., Jenkins A., Okamoto T., 2010, MNRAS, 404, 1137
Biffi V. et al., 2016, ApJ, 827, 112
Bocquet S. et al., 2015, ApJ, 799, 214

Booth C. M., Schaye J., 2009, MNRAS, 398, 53

Bryan G. L., Norman M. L., 1998, ApJ, 495, 80

Bryan S. E., Kay S. T., Duffy A. R., Schaye J., Dalla Vecchia C., Booth C. M., 2013, MNRAS, 429, 3316

Bullock J. S., Dekel A., Kolatt T. S., Kravtsov A. V., Klypin A. A., Porciani C., Primack J. R., 2001, ApJ, 555, 240

Cusworth S. J., Kay S. T., Battye R. A., Thomas P. A., 2014, MNRAS, 439, 2485

Dalla Vecchia C., Schaye J., 2008, MNRAS, 387, 1431

Davis M., Efstathiou G., Frenk C. S., White S. D. M., 1985, ApJ, 292, 371

Duffy A. R., Schaye J., Kay S. T., Dalla Vecchia C., 2008, MNRAS, 390, L64

Duffy A. R., Schaye J., Kay S. T., Dalla Vecchia C., Battye R. A., Booth C. M., 2010, MNRAS, 405, 2161

Dutton A. A., Macciò A. V., 2014, MNRAS, 441, 3359

Einasto J., 1965, Trudy Astrofizicheskogo Inst. Alma-Ata, 5, 87

Foster A. R., Ji L., Smith R. K., Brickhouse N. S., 2012, ApJ, 756, 128

Fukushige T., Makino J., 2001, ApJ, 557, 533

Gao L., Navarro J. F., Cole S., Frenk C. S., White S. D. M., Springel V., Jenkins A., Neto A. F., 2008, MNRAS, 387, 536

Hahn O., Martizzi D., Wu H.-Y., Evrard A. E., Teyssier R., Wechsler R. H., 2015, MNRAS, preprint (arXiv:1509.04289)

Hoekstra H., Herbonnet R., Muzzin A., Babul A., Mahdavi A., Viola M., Cacciato M., 2015, MNRAS, 449, 685

Hopkins P. F., Bahcall N. A., Bode P., 2005, ApJ, 618, 1

Israel H., Reiprich T. H., Erben T., Massey R. J., Sarazin C. L., Schneider P., Vikhlinin A., 2014, A&A, 564, A129

Ivezic Z. et al., 2008, preprint (arXiv:0805.2366)

Jeeson-Daniel A., Dalla Vecchia C., Haas M. R., Schaye J., 2011, MNRAS, 415, L69

Jing Y. P., Suto Y., 2000, ApJ, 529, L69

Kay S. T., Peel M. W., Short C. J., Thomas P. A., Young O. E., Battye R. A., Liddle A. R., Pearce F. R., 2012, MNRAS, 422, 1999

Kettula K. et al., 2015, MNRAS, 451, 1460

Klypin A. A., Trujillo-Gomez S., Primack J., 2011, ApJ, 740, 102

Klypin A., Yepes G., Gottlöber S., Prada F., Heß S., 2016, MNRAS, 457, 4340

Le Brun A. M. C., McCarthy I. G., Schaye J., Ponman T. J., 2014, MNRAS, 441, 1270

Li C., White S. D. M., 2009, MNRAS, 398, 2177

Lieu M. et al., 2016, A&A, 592, A4

Lin Y.-T., Stanford S. A., Eisenhardt P. R. M., Vikhlinin A., Maughan B. J., Kravtsov A., 2012, ApJ, 745, L3

Ludlow A. D., Navarro J. F., Li M., Angulo R. E., Boylan-Kolchin M., Bett P. E., 2012, MNRAS, 427, 1322

McCarthy I. G., Schaye J., Bower R. G., Ponman T. J., Booth C. M., Dalla Vecchia C., Springel V., 2011, MNRAS, 412, 1965

McCarthy I. G., Schaye J., Bird S., Le Brun A. M. C., 2017, MNRAS, 465, 2936

Macciò A. V., Dutton A. A., van den Bosch F. C., Moore B., Potter D., Stadel J., 2007, MNRAS, 378, 55

Macciò A. V., Dutton A. A., van den Bosch F. C., 2008, MNRAS, 391, 1940

Mahdavi A., Hoekstra H., Babul A., Bildfell C., Jeltema T., Henry J. P., 2013, ApJ, 767, 116

Martizzi D., Teyssier R., Moore B., Wentz T., 2012, MNRAS, 422, 3081

Martizzi D., Mohammed I., Teyssier R., Moore B., 2014, MNRAS, 440, 2290

Maughan B. J. et al., 2008, MNRAS, 387, 998

Mazzotta P., Rasia E., Moscardini L., Tormen G., 2004, MNRAS, 354, 10

Meneghetti M. et al., 2014, ApJ, 797, 34

Merritt D., Graham A. W., Moore B., Diemand J., Terzić B., 2006, AJ, 132, 2685

Moore B., Governato F., Quinn T., Stadel J., Lake G., 1998, ApJ, 499, L5

Muñoz-Cuartas J. C., Macciò A. V., Gottlöber S., Dutton A. A., 2011, MNRAS, 411, 584

Nagai D., Vikhlinin A., Kravtsov A. V., 2007, ApJ, 655, 98

Navarro J. F., Frenk C. S., White S. D. M., 1997, ApJ, 490, 493

Navarro J. F. et al., 2004, MNRAS, 349, 1039

Neto A. F. et al., 2007, MNRAS, 381, 1450

Niemack M. D. et al., 2010, Proc. SPIE, 7741, 77411S

Nurgaliev D., McDonald M., Benson B. A., Miller E. D., Stubbs C. W., Vikhlinin A., 2013, ApJ, 779, 112

Oguri M., Hamana T., 2011, MNRAS, 414, 1851

Okabe N., Zhang Y.-Y., Finoguenov A., Takada M., Smith G. P., Umetsu K., Futamase T., 2010, ApJ, 721, 875

Okabe N., Smith G. P., Umetsu K., Takada M., Futamase T., 2013, ApJ, 769, L35

Planck Collaboration XXIX, 2014, A&A, 571, A29

Planck Collaboration XXIV, 2016, A&A, 594, A24

Postman M. et al., 2012, ApJS, 199, 25

Power C., Navarro J. F., Jenkins A., Frenk C. S., White S. D. M., Springel V., Stadel J., Quinn T., 2003, MNRAS, 338, 14

Pratt G. W., Croston J. H., Arnaud M., Böhringer H., 2009, A&A, 498, 361

Rasia E. et al., 2012, New J. Phys., 14, 055018

Rasia E., Meneghetti M., Ettori S., 2013, Astron. Rev., 8, 40

Schaller M. et al., 2015, MNRAS, 451, 1247

Schaye J., Dalla Vecchia C., 2008, MNRAS, 383, 1210

Schaye J. et al., 2010, MNRAS, 402, 1536

Schneider P., Meylan G., Kochanek C., Jetzer P., North P., Wambsganss J., 2006, Gravitational Lensing: Strong, Weak and Micro. Saas-Fee Advanced Course 33, Springer-Verlag, Berlin

Sembolini F. et al., 2016a, MNRAS, 457, 4063

Sembolini F. et al., 2016b, MNRAS, 459, 2973

Simet M., Battaglia N., Mandelbaum R., Seljak U., 2015, Am. Astron. Soc. Meeting Abstr., 225, 443.04

Smith R. K., Brickhouse N. S., Liedahl D. A., Raymond J. C., 2001, ApJ, 556, L91

Smith G. P. et al., 2016, MNRAS, 456, L74

Springel V., White S. D. M., Tormen G., Kauffmann G., 2001, MNRAS, 328, 726

Springel V. et al., 2005, Nature, 435, 629

Stanek R., Rudd D., Evrard A. E., 2009, MNRAS, 394, L11

Sun M., Voit G. M., Donahue M., Jones C., Forman W., Vikhlinin A., 2009, ApJ, 693, 1142

The Dark Energy Survey Collaboration, 2005, preprint (astro-ph/0510346)

Velliscig M., van Daalen M. P., Schaye J., McCarthy I. G., Cacciato M., Le Brun A. M. C., Dalla Vecchia C., 2014, MNRAS, 442, 2641

Vikhlinin A., Kravtsov A., Forman W., Jones C., Markevitch M., Murray S. S., Van Speybroeck L., 2006, ApJ, 640, 691

von der Linden A. et al., 2014a, MNRAS, 439, 2

von der Linden A. et al., 2014b, MNRAS, 443, 1973

Wiersma R. P. C., Schaye J., Smith B. D., 2009, MNRAS, 393, 99

Wilcox H. et al., 2015, MNRAS, 452, 1171

Wright C. O., Brainerd T. G., 2000, ApJ, 534, 34

Zemp M., Gnedin O. Y., Gnedin N. Y., Kravtsov A. V., 2011, ApJS, 197, 30

Zhang Y.-Y. et al., 2010, ApJ, 711, 1033

This paper has been typeset from a T_EX/L^AT_EX file prepared by the author.